«ФИЗИКА ЭЛЕМЕНТАРНЫХ ЧАСТИЦ И АТОМНОГО ЯДРА»
1999, ТОМ 30, ВЫП. 4

УДК 539.17, 539.16.01

COLD FISSION MODES IN ^{252}Cf

A.Săndulescu, Ş.Mişicu, F. Carstoiu

National Institute for Nuclear Physics, Bucharest P.O.Box MG-6, Romania

W.Greiner

Institut für Theoretische Physik der J.W.Goethe Universität, Frankfurt am Main, Germany

«ФИЗИКА ЭЛЕМЕНТАРНЫХ ЧАСТИЦ И АТОМНОГО ЯДРА»
1999, ТОМ 30, ВЫП. 4

УДК 539.17, 539.16.01

COLD FISSION MODES IN ^{252}Cf

A.Săndulescu, Ş.Mişicu, F. Carstoiu

National Institute for Nuclear Physics, Bucharest P.O.Box MG-6, Romania

W.Greiner

Institut für Theoretische Physik der J.W.Goethe Universität, Frankfurt am Main, Germany

The binary and ternary cold fragmentations of heavy nuclei are studied in the frame of a deformation dependent cluster model where the final fragments are born to their respective ground states and interact via a double-folded potential with M3Y forces. The deformation effects are taken into account up to a multipolarity $\lambda = 4$. We show that two regions of cold fragmentation arise. The first one has large quadrupole and even hexadecupole deformations and mass number of the heavy fragment ranging between 138 and 158. In the second region, the Q-value principle dictates the occurrence of a few spherical nuclei around the double magic ^{132}Sn, similar to the case of heavy cluster radioactivity, where the daughter nuclei are around ^{208}Pb. This structure is similar for both binary and ternary cold fission. We compute the cold fission yields for the binary fragmentation and for the alpha-accompanied fission of ^{252}Cf. For the ternary cold fission mode we derive the most likely geometrical and dynamical characteristics of the fragments at the release moment of the light particle and perform classical trajectory calculations, in order to compute the final kinetic energy of the alpha particle. The recent observation of ^{10}Be in the cold ternary fission is discussed in conjunction with the concept of giant nuclear molecule.

Исследована двойная и тройная холодная фрагментация тяжелых ядер в рамках кластерной модели с учетом деформации. Предполагалось, что конечные фрагменты рождаются в соответствующих основных состояниях и взаимодействуют при помощи потенциала двойной свертки с $M3Y$-силами. Эффекты деформации учитывались вплоть до мультипольности $\lambda = 4$. Показано, что возникают две области холодной фрагментации. Первой области отвечают большие квадрупольные и даже гексадекапольные деформации и массовые числа тяжелых фрагментов в диапазоне от 138 до 158. Во второй области выделяется случай небольшого числа сферических ядер в окрестности дважды магического ^{132}Sn, подобный распаду на тяжелые кластеры, при котором дочерние ядра лежат в окрестности ^{208}Pb. Эта структура одинакова для случаев двойного и тройного холодного деления. Рассчитан выход холодного деления ^{252}Cf для бинарной фрагментации и сопутствующего альфа-распада. Для тройной моды холодного деления получены наиболее вероятные геометрические и динамические характеристики фрагментов при выделенном моменте легкой частицы и проведен расчет классической траектории с целью получения конечной энергии альфа-частицы. Обсуждаются недавние наблюдения ^{10}Be в холодном тройном делении в связи с концепцией гигантских ядерных молекул.

1. INTRODUCTION

Rare decays ranging from the emission of heavy clusters having masses between A_L = 14 and 34 [1, 2], up to the cold (neutronless) fission of many

actinide nuclei which produce fragments with $\approx$ 70 to $\approx$ 166 atomic mass units were observed in the last decade [3–9]. All these fragmentation processes are confirming the theoretical predictions based on the idea of the cold rearrangements of large groups of nucleons from the ground state of the initial nucleus to the ground states of the two or three final fragments [1, 10].

Milton and Fraser [11] were the first who noticed that a small percentage of the fission fragments are produced predominantly at high kinetic energies so that those nuclei are formed nearly in their ground-state. Later on, Signarbieux et al. [12] confirmed the previous interpretation by determining the mass distributions of the primary fragments for the highest values of the kinetic energy. They concluded that even before the scission takes place we deal with a superposition of two fragments in their ground state, from which the *cold (neutronless) fragmentation* term emerged. In all these situations the final fragments have compact shapes at the scission point and almost zero excitation energy. In the hypothesis that the cold(neutronless) fragmentation is the tail of the fission mass distribution, it has been shown that the transitions from the fission valley to the fusion valley along the fission path can qualitatively explain the cold fragmentation of the actinides [13]. On the other hand the deformation dependent cluster model for cold fission, similar to the one for cluster radioactivity [1], where the ground state deformations of the final fragments are a very important ingredient [14, 15], is able to explain quantitatively the mass and charge experimental yields [16]. Thus the cold fission is viewed as an extension of cluster radioactivity.

The first direct observation of cold (neutronless) binary fragmentations in the spontaneous fission of ^{252}Cf was recently made [5, 6] by using the multiple Ge-detector Compact Ball facility at Oak Ridge National Laboratory, and more recently with the early implementation of Gammasphere [7]. Also the first evidence for cold (neutronless) ternary fission where the third particle is an α particle was very recently reported [17]. All these data were obtained in studying the spontaneous fission of ^{252}Cf with Gammasphere by using the triple coincidence technique. We notice that the probability for neutronless fission is 0.0021 ± 0.0008 for ^{252}Cf.

Very recently, average angular momentum for primary fission fragments as a function of neutron multiplicity were extracted for the first time for the Mo-Ba and Zr-Ce charge splits of ^{252}Cf [18]. It was found that for the major part of fission events characterized by close to the average numbers of emitted neutrons (ν_{tot} = 2-5), bending oscillations are excited to the temperature of 2—3 MeV which implies a weak coupling between collective and internal degrees of freedom from descent to the scission point.

In this review paper we present a deformation dependent cluster model for the cold (neutronless) binary and ternary fission of ^{252}Cf. We use only the penetrabilities through the potential barrier and neglect the cluster preformation factors. For the evaluation of the potential barriers between the final fragments

we used the M3Y nucleon-nucleon forces. We found that the binary and ternary isotopic yields are very sensitive to the deformations of fragments and especially to the hexadecupole term.

Also we study the final characteristics of the light particle emitted in the α-accompanied ternary cold fission of ^{252}Cf.

A short section is devoted to the recent observation of ^{10}Be accompanying the ternary cold fission.

2. DOUBLE FOLDING POTENTIAL BARRIER

In order to compute the cold fission barriers we employ a cluster model similar to the one-body model used for the description of cluster radioactivity [1]. The initial nucleus is assumed to be already separated in two fragments or into two heavier fragments and a light cluster, for the cold binary fission and the cold ternary fission, respectively. Consequently we define the binary(ternary) fission barrier as the sum of interaction energies V_{ij} between the two(three) fragments

$$V = \sum_{i>j} V_{ij}(\mathbf{R}_{ij}). \tag{1}$$

The above heavy-ion interactions depend on the centre-to-centre distances, R_{ij}, and on the relative orientation Ω_1 and Ω_2 as we shall see below. In the most simple case, that of the binary fission, only one term will be involved in the above definition whereas for a multifragmentation process, when more than two nuclei are emerging from the reaction, some constraints should be imposed on the relative positions $\mathbf{R}_{ij}$. In the chapter devoted to the ternary fission this question will be addressed in detail.

The advantage of such a model is that the barrier between the fragments can be calculated quite accurately due to the fact that the touching configurations are situated inside of the barriers. Moreover the shapes of the fragments are constant at every stage of the fission. The Q values and the deformation parameters contain all nuclear shell and pairing effects of the corresponding fragments.

We evaluated the interaction between two deformed fragments $V(\mathbf{R})$ as the sum of the short-range nuclear interaction $V_N(\mathbf{R})$ and the long-range Coulomb $V_C(\mathbf{R})$ parts. It can be calculated as the double folding integral of ground state one-body densities [19]

$$V(\mathbf{R}) = \int d\mathbf{r}_1 d\mathbf{r}_2 \rho_1(\mathbf{r}_1)\rho_2(\mathbf{r}_2)v(\mathbf{r}_{12}). \tag{2}$$

The ground state one-body nuclear densities of the fragments are taken as Fermi

distributions in the intrinsic frame

$$\rho(\mathbf{r}) = \rho_0 \left[1 + \exp \frac{1}{a} \left(r - R_0 \left(1 + \sum_{\lambda=2,3,4} \beta_\lambda Y_{\lambda 0}(\theta, 0) \right) \right) \right]^{-1}. \quad (3)$$

The constant ρ_0 is fixed by normalizing the proton and neutron density to the Z proton and N neutron numbers, respectively. This condition ensures the volume conservation. The radius R_0 and diffusivity parameters were taken from the liquid drop model [20]. Only static axial symmetric deformations were considered in our calculations. However, possible triaxial configurations for the nuclei emerging in the cold fission of ^{252}Cf should not be discarded.

The double folded potential barrier for two final nuclei with orientation in space given through the Euler angles Ω_1 and Ω_2 is computed by making a general multipole expansion [21, 22].

$$V(\mathbf{R}, \Omega_1, \Omega_2) = \sum_{\lambda_i, \mu_i} V^{\mu_1 \mu_2 \mu_3}_{\lambda_1 \lambda_2 \lambda_3}(R) D^{\lambda_1}_{\mu_1 0}(\Omega_1) D^{\lambda_2}_{\mu_2 0}(\Omega_2) Y_{\lambda_3 \mu_3}(\hat{R}). \quad (4)$$

Here, $D^{\lambda_1}_{\mu_1 0}(\Omega_1)$ and $D^{\lambda_2}_{\mu_2 0}(\Omega_2)$ are the Wigner rotation matrices describing the relative orientation of the two fragments, whereas $Y_{\lambda_3 \mu_3}(\hat{R})$ describes the orientation of the axis joining the two nuclei with respect to the laboratory frame. For the case with both final fragments aligned along the same symmetry axis ($\hat{R}$ = (0, 0), $\Omega_1 = \Omega_2 =$ (0, 0, 0)) we obtain

$$V(R) = \sum_{\lambda_i} V^{0\ 0\ 0}_{\lambda_1 \lambda_2 \lambda_3}(R) \quad (5)$$

with

$$V^{0\ 0\ 0}_{\lambda_1 \lambda_2 \lambda_3}(R) = \frac{2}{\pi} \left(C^{\lambda_1 \lambda_2 \lambda_3}_{0\ 0\ 0} \right)^2 \int r_1^2 dr_1 r_2^2 dr_2 \ \rho_{\lambda_1}(r_1) \rho_{\lambda_2}(r_2) F_{\lambda_1 \lambda_2 \lambda_3}(r_1, r_2, R), \quad (6)$$

where $C^{0\ 0\ 0}_{\lambda_1 \lambda_2 \lambda_3}$ is a Clebsch–Gordan coefficient. Above we have introduced the double folding kernel

$$F_{\lambda_1 \lambda_2 \lambda_3}(r_1, r_2, R) = \int q^2 dq \ \tilde{v}(q) j_{\lambda_1}(q r_1) j_{\lambda_2}(q r_2) j_{\lambda_3}(q r_3), \quad (7)$$

where $\tilde{v}(q)$ denotes the Fourier transform of the effective interaction and j_λ are spherical Bessel functions. The quantities ρ_λ are the multipole components of the corresponding expansion of the nuclear densities

$$\rho(\mathbf{r}) = \sum_{\lambda=0,2,3,4} \rho_\lambda(r) Y_{\lambda 0}(\hat{r}). \quad (8)$$

The selection rules for the angular momentum coupling give $\lambda_1 + \lambda_2 + \lambda_3$ =even. When $\beta_\lambda \neq 0$, $\lambda = 2, 3, 4$ for both fragments, then the sum in (5) involves 32 terms for a nose-to-nose configuration and $\lambda_3 \leq 6$. Special care has been payed to obtain numerically the integrals involved in expressions (6), (7). For most of the fragmentation channels studied here, large quadrupole, hexadecupole, and occasionally octupole deformations are involved. Therefore a Taylor expansion method for obtaining the density multipoles cannot be considered. On the other hand, a large quadrupole deformation induces according to (8) non-vanishing multipoles with λ=4 and 6 even if β_4=β_6=0. Therefore for a correct calculation of ρ_λ, a numerical method with a truncation error of order O(h^7) is needed in order to ensure the orthogonality of spherical harmonics with $\lambda \leq 6$.

Performing the integrals (6) and (7) we have used a numerical method with a truncation error of the order O(h^9). All short range wavelength ($q \leq 10$ fm^{-1}) have been included and particular care has been taken to ensure the convergence of the integrals with respect to the integration step and the range of integration.

The asymptotic part of the barrier is determined essentially by the Coulomb multipoles which are obtained also as double folding integrals involving charge densities. For $R >> r_1 + r_2$, the Coulomb kernel in (7) behaves as [22]

$$F^C_{\lambda_1\lambda_2\lambda_3}(r_1, r_2, R) = 2\pi^2 \frac{(2\lambda_3+1)!!}{(2\lambda_3+1)(2\lambda_1+1)!!(2\lambda_2+1)!!} \frac{r_1^{\lambda_1} r_2^{\lambda_2}}{R^{\lambda_3+1}} \delta_{\lambda_3,\lambda_1+\lambda_2}. \quad (9)$$

If we introduce the moments of the charge density as

$$Q_\lambda = \sqrt{\frac{4\pi}{2\lambda+1}} \int_0^\infty r^2 dr \rho_\lambda(r) r^\lambda, \quad (10)$$

where $Q_0 = Z$ (atomic number), then the $\lambda_3 = 2$ component of function (6) behaves for $R \to \infty$ as

$$\frac{Z_1 Q_2^2 + Z_2 Q_2^1}{R^3}. \quad (11)$$

First we have chosen the M3Y effective interaction [23] which is representative for the so-called local and density independent effective interactions [24]. This interaction is particularly simple to use in folding models since it is parametrized as a sum of 3 Yukawa functions in each spin-isospin (S, T) channel. The spin-spin v_{10} and spin-isospin v_{11} components are disregarded since for a lot of fragments involved in the calculation the ground state spins are unknown. The spin-spin component of the heavy-ion potential can be neglected here, as it is of the order of $1/A_1A_2$. Only the isoscalar and isovector components have been

retained in the present study for the central heavy ion interaction:

$$v(\mathbf{r}_{12}) = v_{00}(\mathbf{r_{12}}) + \hat{J}_{00}\delta(\mathbf{r}_{12}) + (v_{01}(\mathbf{r_{12}}) + \hat{J}_{01}\delta(\mathbf{r}_{12}))\vec{\tau}_1 \cdot \vec{\tau}_2 + \frac{e^2}{r_{12}}, \quad (12)$$

where

$$\mathbf{r}_{12} = \mathbf{R} + \mathbf{r}_2 - \mathbf{r}_1. \quad (13)$$

The isoscalar component of the M3Y force is

$$v_{00}(r) = \left[\ 7999 \ \frac{e^{-4r}}{4r} - 2134 \ \frac{e^{-2.5 \ r}}{2.5 \ r} \right] \quad \text{MeV},$$

and the isovector part has the form

$$v_{01}(r) = \left[\ -4885.5 \ \frac{e^{-4r}}{4r} + 1175.5 \ \frac{e^{-2.5 \ r}}{2.5 \ r} \right] \quad \text{MeV}.$$

The M3Y interaction is dominated by the one-nucleon knock-on exchange term which leads to a nonlocal kernel. In Eq.(12) the nonlocal potential is reduced to a zero range pseudopotential $\hat{J}_{00}\delta(\mathbf{r}_{12})$, with a strength depending slightly on the energy. This is due to the fact that the range of the nonlocality behaves as μ^{-1}, where $\mu = A_1A_2/(A_1 + A_2)$ is the reduced mass of the fragments. We have used the common prescription [24] $\hat{J}_{00}$ = -276 MeV·fm^3 neglecting completely the small energy dependence. For example, the odd-even staggering in the Q value for a fragmentation channel, which is typically of the order of ΔQ = 2 MeV, leads to a variation $\Delta\hat{J}_{00}$=-0.005$\frac{\Delta Q}{\mu}$ MeV·fm^3 with $\mu \approx$60. The isovecor component in Eq.(12) with a strength $\hat{J}_{01}$ = 217 MeV $\cdot$ fm^3 for the pseudoexchange term, gives a small repulsive contribution in the barrier region.

As we shall show later, employing M3Y NN effective interactions proved to be satisfactory for the computation of the WKB penetrabilities for the binary and ternary cold fission of ^{252}Cf, when only the region in the vicinity of the barrier is important. However, the M3Y double-folded potential is not taking into account two major factors - the density dependence of the NN interaction and the Pauli principle, which are important at distances corresponding to the overlap of the nuclear volumes. This potential is characterized by a strong, unphysical attraction of a few thousands of MeV inside the nucleus. To accomodate a repulsive core which would prevent the reabsorbtion of the lighter fragment by the heavier one we subsequently introduced a double folding potential based on the effective Skyrme interaction. This is a good choice for a decaying giant molecule or dinuclear system [25, 26] in view of its similarities with the inter-atomic potentials used in the physics of the molecule [27]. Thus the nuclear potential between two ions contains an attractive part and a repulsive one. Neglecting the

spin dependence, it can be written as

$$V_N(\mathbf{R}) = C_0 \left\{ \frac{F_{in} - F_{ex}}{\rho_{00}} \left((\rho_1^2 * \rho_2)(\mathbf{R}) + (\rho_1 * \rho_2^2)(\mathbf{R}) \right) + F_{ex}(\rho_1 * \rho_2)(\mathbf{R}) \right\}, \tag{14}$$

where $*$ denotes the convolution of two functions f and g, i.e., $(f * g)(\mathbf{x}) = \int f(\mathbf{x}')g(\mathbf{x}-\mathbf{x}')d\mathbf{x}'$. The constant C_0 and the dimensionless parameters F_{in}, F_{ex} are given in Ref.25. To solve this integral we consider the inverse Fourier transform

$$V_N(\mathbf{R}) = \int e^{-i\mathbf{q}\cdot\mathbf{R}} \widetilde{V}_N(\mathbf{q}) d\mathbf{q}, \tag{15}$$

where the Fourier transform of the local Skyrme potential $\widetilde{V}_N(\mathbf{q})$ can be casted in the form

$$\widetilde{V}_N(\mathbf{q}) = C_0 \left\{ \frac{F_{in} - F_{ex}}{\rho_{00}} \left(\widetilde{\rho}_1^2(\mathbf{q})\widetilde{\rho}_2(-\mathbf{q}) + \widetilde{\rho}_1(\mathbf{q})\widetilde{\rho}_2^2(-\mathbf{q}) \right) + F_{ex}\widetilde{\rho}_1(\mathbf{q})\widetilde{\rho}_2(\mathbf{q}) \right\}. \tag{16}$$

Here $\widetilde{\rho}(\mathbf{q})$ and $\widetilde{\rho^2}(\mathbf{q})$ are Fourier transforms of the nucleon densities $\rho(\mathbf{r})$ and squared nuclear densities $\rho^2(\mathbf{r})$. Then [26]

$$\widetilde{\rho}(\mathbf{q}) = 4\pi \sum_{\lambda} i^{\lambda} Y_{\lambda 0}(\theta_q, 0) \int_0^{\infty} r^2 dr \rho_{\lambda}(r) j_{\lambda}(qr), \tag{17}$$

$$\widetilde{\rho^2}(\mathbf{q}) = \sqrt{4\pi} \sum_{\lambda} \frac{i^{\lambda}}{\hat{\lambda}} Y_{\lambda 0}(\theta_q, 0) \sum_{\lambda'\lambda''} \hat{\lambda}'\hat{\lambda}'' (C^{\lambda\lambda'\lambda''}_{0\,0\,0})^2 \times$$
$$\times \int_0^{\infty} r^2 dr \rho_{\lambda'}(r)\rho_{\lambda''}(r) j_{\lambda}(qr). \tag{18}$$

3. THE COLD BINARY FISSION

We start the study of the binary cold fission, by assuming that at scission, the two deformed fragments are coaxial and their poles are almost touching like in the tip model [15]. For quadrupole deformations we choose prolate spheroids since the prolate shapes are favoured in fission. Also, it is known that in the potential energy surfaces of nuclei with masses $100 \leq A \leq$ for each 130, oblate minimum always corresponds another prolate minimum close in energy. For pear shapes, i.e., fragments with quadrupole and octupole deformations, we choose opposite signs for the octupole deformations, i.e., nose-to-nose configurations (see Fig.1). For hexadecupole deformations we choose only positive signatures, because they lead to a lowering of barriers in comparison with the negative ones and consequently such configurations are much more favoured in fission (see Fig.2).

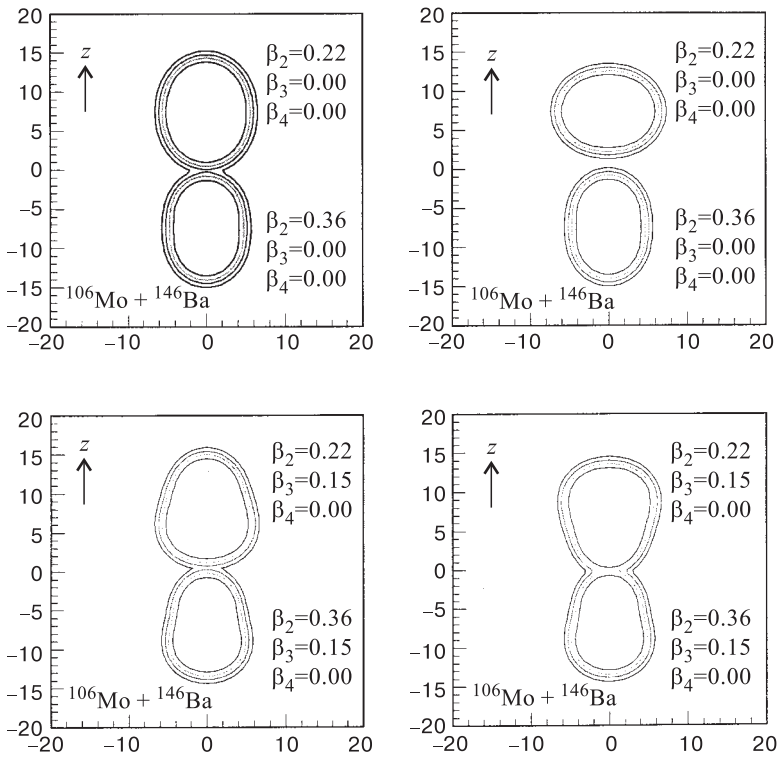

Fig. 1. Density plots of ^{106}Mo and ^{146}Ba fragments, placed at R=15 fm, considered with quadrupole and octupole deformations. In the upper part are represented the prolate-prolate, oblate-prolate positions and in the lower part two pear shapes — nose-to-back and nose-to-nose. The penetrability is maximized for $\beta_2 > 0$ configurations

In order to illustrate the influence of deformations on the barriers we displayed in Fig.3 the M3Y-folding multipoles for ^{106}Mo interacting with ^{146}Ba, with all deformations included. The octupole component is large in the interior but gives negligible contribution in the barrier region in contrast to the hexadecupole one. Next, in Fig.4 we are illustrating for the same partners the cumulative effect of high rank multipoles on the barrier.

In the laboratory frame of reference the x axis was taken as the initial fissioning axis of the two heavy fragments, with the origin at their point of contact. The potential barriers $V_{LH} - Q_{LH}$ between the two fragments are high but rather thin with a width of about 2 to 3 fm. As an illustration, we show in Fig.5 a typical barrier between ^{146}Ba and ^{106}Mo, as a function of the distance R_{LH} between their centres of mass. Here Q_{LH} is the decay energy for the binary

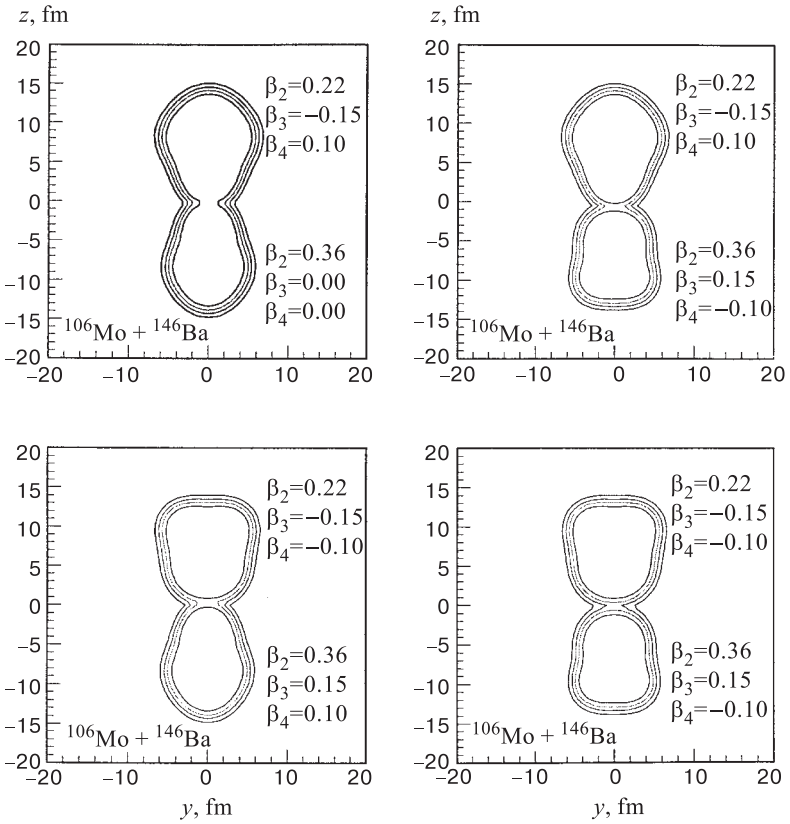

Fig. 2. Same as for Fig.1. The influence of different signs of hexadecupole deformations on ^{106}Mo and ^{146}Ba densities in the presence of large quadrupole and octupole deformations. The penetrability is maximized for $\beta_4 > 0$ configurations

fragmentation of ^{252}Cf. For the two fragments, the exit point from their potential barrier is at R_{LH} typically between 16 and 17 fm which supports our cluster model.

Note that in the cluster model, employed in this paper, the preformation factors for different channels are neglected, i.e., we use the same assault frequency factor ν for the collisions with the fission barrier for all fragmentations. It is generally known that the general trends in alpha decay of heavy nuclei are very well described by barrier penetrabilities, the preformation factors becoming increasingly important only in the vicinity of the double magic nucleus ^{208}Pb. In the present approach to cold binary fragmentation of ^{252}Cf the preformation factors are taken to be constant. However in this case too, as we shall see

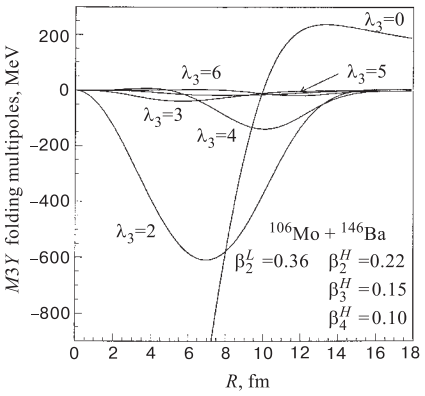

Fig. 3. The influence of the M3Y-folding multipoles on the barrier between ^{106}Mo and ^{146}Ba. Notice that the main effect is due to $\lambda_3 = 2$. The influence of $\lambda_3 = 3$ is large but less important in the barrier region compared with the induced deformations $\lambda_3 = 5$ and $\lambda_3 = 6$

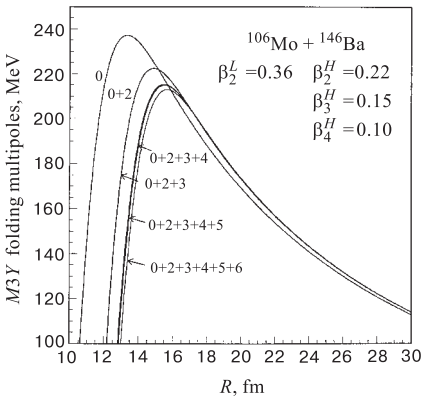

Fig. 4. The cumulative effect of high rank multipoles on the barrier between ^{106}Mo and ^{146}Ba. We considered the deformations β_3 and β_4 much larger than the real ones in order to illustrate the effect of deformations

later, around the double-magic nucleus ^{132}Sn the preformation turns out to be of capital importance. Eventually, as the experimental data become more accurate one could extract some fragment preformation factors and discuss the related nuclear structure effects.

The penetrabilities through the double-folded potential barrier between the two heavy fragments were calculated by using the WKB approximation

$$P = \exp\left\{-\frac{2}{\hbar}\int_{s_i}^{s_o}\sqrt{2\mu\,[\,V_F(s) - Q_{LH}\,]}\;\;ds\right\}, \tag{19}$$

where s is the relative distance, μ is the reduced mass and s_i and s_o are the inner and outer turning points, defined by $V_F(s_i) = V_F(s_o) = Q_{LH}$.

The barriers were computed with the Liquid Drop Model (LDM) parameters $a_p = a_n$=0.5 fm, $r_{0p} = r_{0n} = (R - \frac{1}{R})A^{-1/3}$ fm with $R = 1.28A^{1/3} + 0.8A^{-1/3} - 0.76$.

Accurate knowledge of Q values is crucial for the calculation, since the WKB penetrabilities are very sensitive to them. We obtained the Q values from experimental mass tables [28], and for only a few of the fragmentations the nuclear masses were taken from the extended tables of Möller et al. [20] computed using the macroscopic-microscopic model.

Let us consider for the beginning only the relative isotopic yields corresponding to true cold (neutronless) binary fragmentations in which all final nuclei

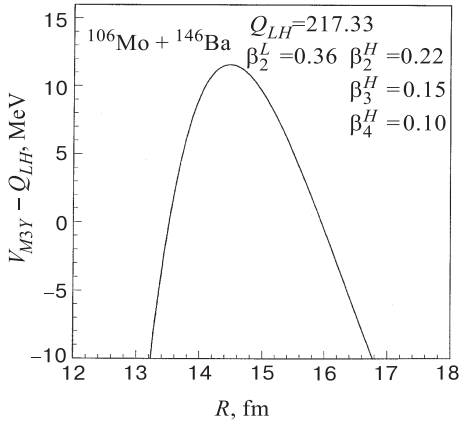

Fig. 5. The barrier between ^{146}Ba and ^{106}Mo as a function of the distance R_{HL} between their centres of mass. Q_{LH} is the decay energy

are left in their ground state. These relative isotopic yields are given by the expression ($A_1 = A_L, A_2 = A_H$)

$$Y(A_1, Z_1) = \frac{P(A_1, Z_1)}{\sum_{A_1 Z_1} P(A_1, Z_1)} \quad . \tag{20}$$

As we mentioned above, the fragment deformations were chosen to be the ground state deformations of Möller et al. [20], computed in the frame of the macroscopic-microscopic model. In Fig.6 we represented separately these deformations for the light A_L and heavy A_H fragments for odd and even charge Z. We can see that the light fragments have mainly quadrupole deformations in contrast to the heavy fragments, which have all types of deformations. The octupole deformations are nonzero in a small heavy fragment mass number region $141 \leq A_H \leq 148$. The fragments with mass number $A_L \leq 92$ and $A_H \leq 138$ are practically spherical.

The computed M3Y-fission barriers heights, for different assumptions: no deformations, including the quadrupole ones, including the quadrupole and octupole ones and for all deformations, together with the corresponding Q values are represented in Fig.7 for odd Z and even Z separetely. We notice the large influence due to the quadrupole deformations, but also the hexadecupole ones are lowering the barriers very much. The octupole deformations in the mass region $141 \leq A_H \leq 148$ have a smaller effect then we expected. This is an illustration of the difference between cluster radioactivity, which is due only to the large Q values and the cold fission which is due mainly to the lowering of the barriers by the fragment deformations. Both processes are cold fragmentation phenomena.

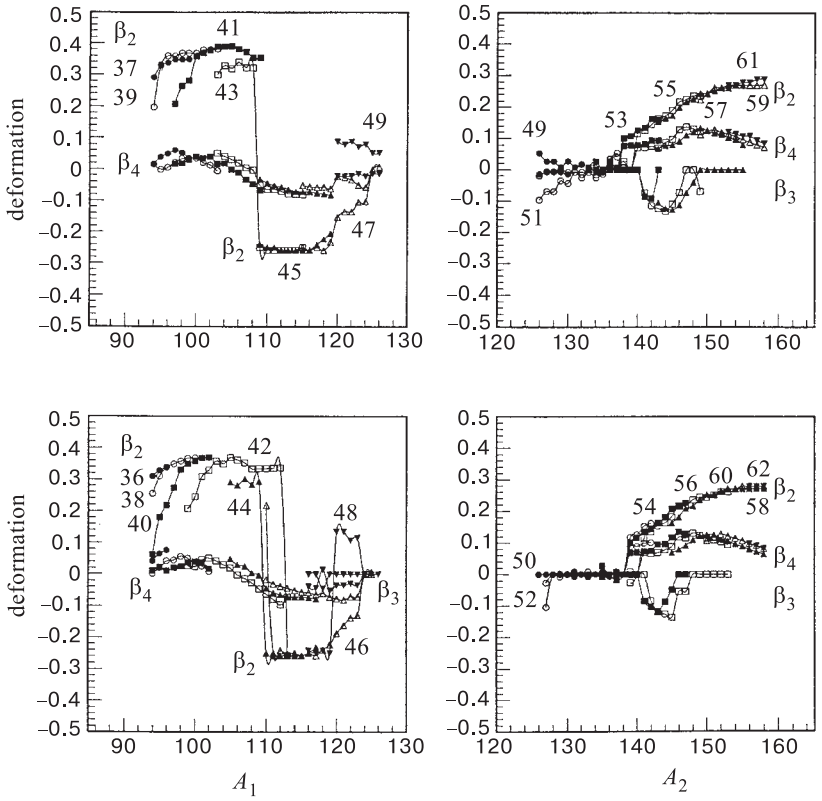

Fig. 6. The assumed β_2, β_3, β_4 ground state fragment deformations are represented by symbols along an isotopic chain labelled by the charge number. The light fragments (Z_1, A_1) have mainly quadrupole deformations in contrast to the heavy fragments (Z_2, A_2). The octupole deformations are existing in a small mass region $141 \leq A_2 \leq 148$, whereas the hexadecupole deformations are important in the region $138 \leq A_2 \leq 158$. The fragments with masses $A_1 \leq 94$ and $A_2 \leq 138$ are practically spherical

The computed yields in percents, for the splittings represented by their fragment deformation parameters in Fig.6 or by their barrier heights in Fig.7, are given in Fig.8 for spherical fragments ($\beta_i = 0$), for quadrupole deformations (β_2), and for all deformations ($\beta_2 + \beta_3 + \beta_4$) at zero excitation energy. We can see that when the fragments are assumed to be spherical the splittings with the highest Q values, which correspond to real spherical heavy fragments(see Fig.6), i.e., for charge combinations $Z_1/Z_2 = 48/50$, 47/51, and 46/52 are the predominant ones. This situation is encountered also in with the cluster radioactivity where the governing principle is the Q value. Due to the staggering of Q values (see Fig.7) the highest yields are for even-even splittings. By including the β_2 deformations

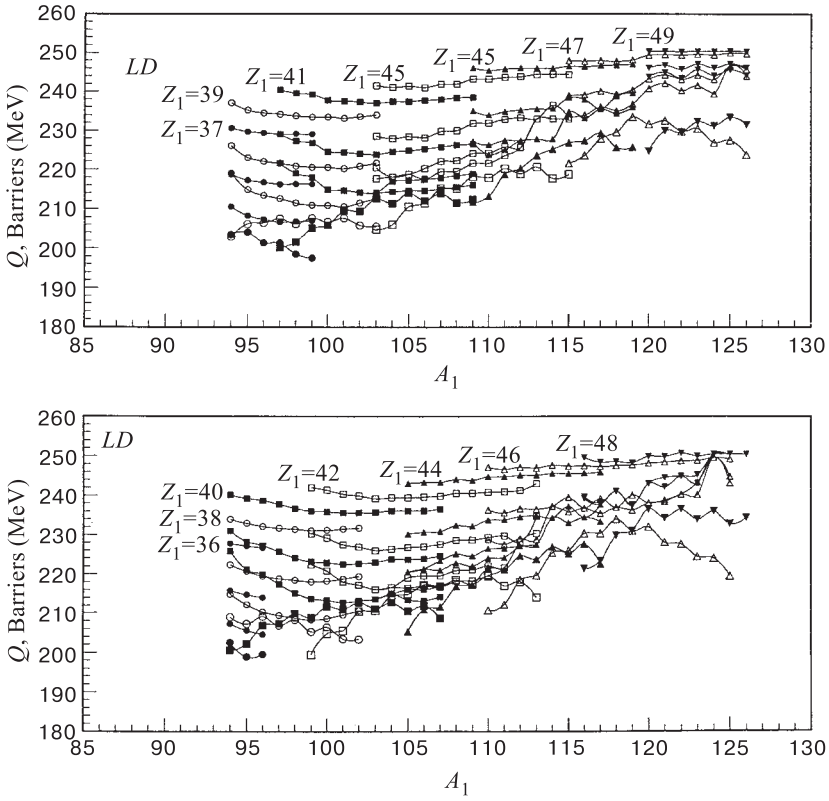

Fig. 7. The barrier heights for all considered fragmentation channels represented for different charges Z_L and mass numbers A_L of the light fragment. The Q values are represented by slightly larger symbols

few asymmetric splittings arise. For all deformations more asymmetric yields appear. Now the principal yields are for Z_1/Z_2= 38/60, 40/58, 41/57, and 42/56 along with 44/54, 46/52, and 47/51. It is a direct consequence of the fact that the influence of the fragment deformations on the yields overcome the influence of Q values in the more asymmetric region. This illustrates the fact that cold fission is a cold rearrangement process in which all deformations are playing the main role and not the Q values. The staggering for odd Z fragmentations like Z_1/Z_2 = 39/59, 41/57, 43/55, 45/53, and 47/51 or odd N fragmentations is recognized at first glance. However, by the introduction of the density levels this staggering is reversed. The largest yields will be for odd Z and/or N fragmentations.

In the next figure we represent the mass yields $Y_{A_2} = \sum_{Z_2} Y(A_2, Z_2)$ (Fig.9) for spherical fragments (β_i=0), for quadrupole deformations ($\beta_2 \neq 0$), and for all

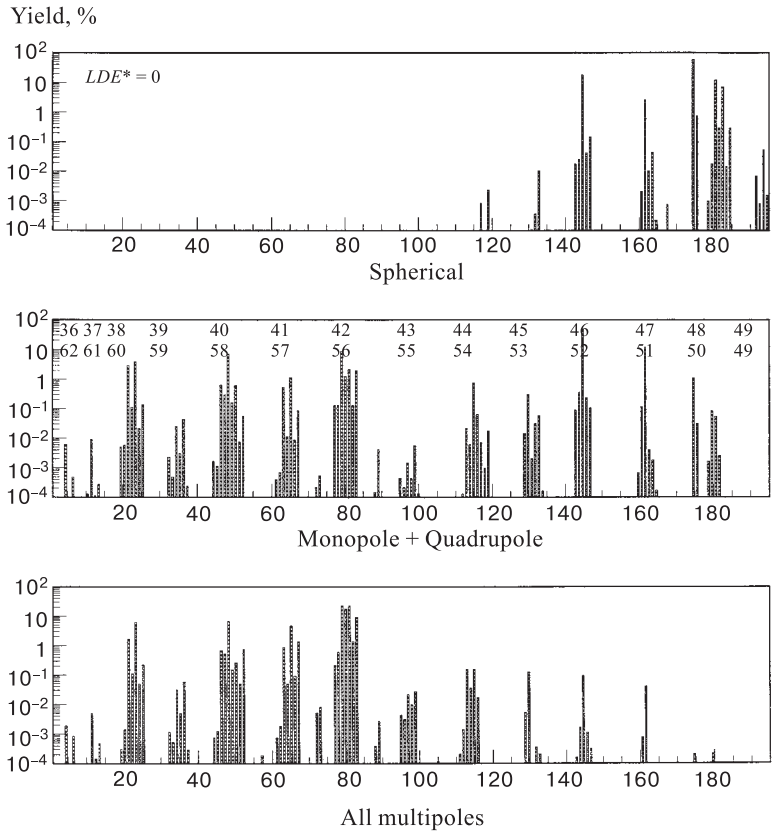

Fig. 8. The true cold fission yields calculated with LDM parameters at zero excitation energy. Results with all deformation turned off are represented in the upper panel, with inclusion of quadrupole deformations on the middle and with all deformations on the bottom. Each group of splittings is labeled by charge combination Z_L/Z_H on the top of the middle panel. Numbers on the horizontal axis represent the ordering of fragmentation channels

deformations ($\beta_i \neq 0$). We can see in the spherical case that the main mass yields are centered around A_2=132. All these heavy fragments are spherical or nearly spherical (with a small prolate deformation) and have high-Q values. Since other spherical fragments do not arise in the yields diagram it occurs that in the spherical case the Q value is the dictating principle. When we turn on the quadrupole deformation a rearrangement in this spherical region takes place. The yield corresponding to A_2=132 is still important, but the one for A_2=134 takes over, although the maximum decay energy of the first mass split Q_{max} is larger

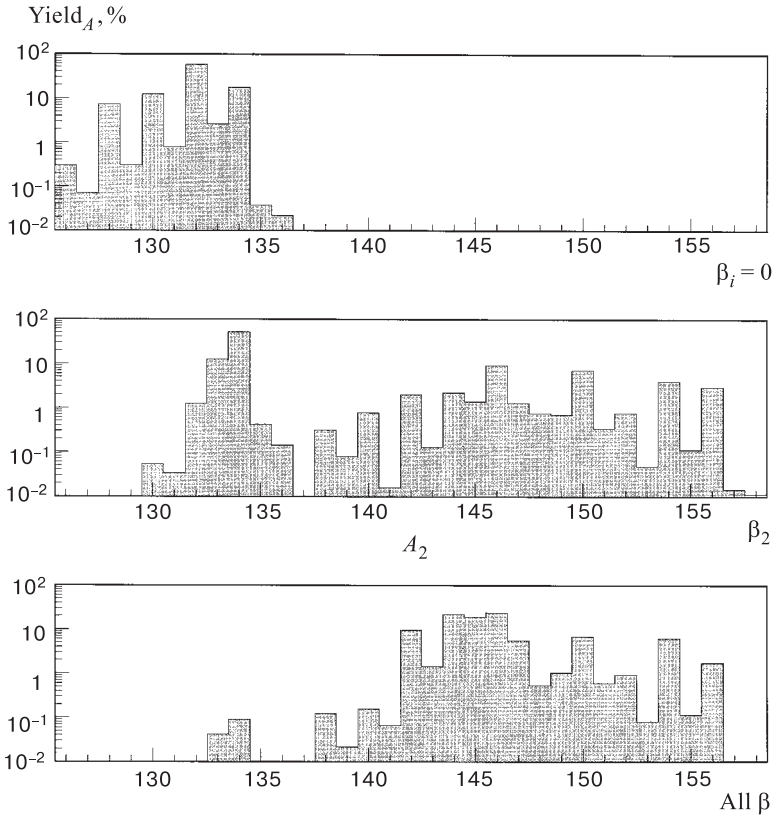

Fig. 9. The mass yields $Y_{A_H} = \sum_{Z_H} Y(A_H, Z_H)$ in percents, as a function of heavy fragment mass computed with LDM parameters. Calculatio ns without deformations ($\beta_{2,3,4}$=0) enhance only the spherical region $A_H \leq 136$; the inclusion of quadrupole deformations ($\beta_2 \neq 0$) enhances the yield with $A_H = 134$; for all deformations there are two main mass yields regions, i.e., $132 \leq A_H \leq 136$ and $138 \leq A_H \leq 156$

than that of the former. In this case the larger quadrupole deformation of the light partner decides the augmentation of the A_2=134 yield. When we include the higher multipole deformations, i.e., octupole and hexadecupole deformations, the yields diagram will change drastically over the whole mass range. First of all, in the spherical region the mass-splittings yields A_2=132, 134 are lowered whereas their odd neighbours are augmented. This is a consequence of the fact that the hexadecupole deformations of the odd light partners are slightly larger. But the most important change occurs in the mass region A_2=138÷156 where a whole bunch of splittings show up with yields greater than 0.01%. This is, beyond any doubt, an effect due to the hexadecupole deformations. As can be inferred from

Fig.6 the above-mentioned mass region is characterized by noticeable values of the hexadecupole deformation. Before adding the hexadecupole deformation, this region has very low yields whereas after the inclusion of β_4 the most pronounced peaks are A_2= 142, 144-147, 150, and 154. It is the right place to mention that these two mass regions obtained by us employing a deformation dependent cluster model of cold fission were also reported by the Tbingen [29–31]. The ranges are almost identical. However in order to reproduce completely the experimental data we have to underline the elements that have to be supplied further in our model. First, in the spherical region, the experiment claims a mass region of cold fission centered around A_2=132, instead of A_2=134 as we obtained. However this misfit was to be expected since we didn't include the preformation factors. In the case of the doubly magic nucleus ^{132}Sn this assumption proves to be unsatisfactory. As has been advocated by the Tübingen group [30] this is a possible manifestation of heavy-cluster decay. Therefore it is very likely that in this case the preformation factor, which multiplies the penetrability, is larger for ^{132}Sn than for the neighbouring nuclei, which could then account for the discrepancies between our calculations and experimental data. However, an encouraging experimental point which supports our calculations is the fact that the even masses 134 and 136 are accompanying the leading yield for 132. In Fig.10 we compare the total yields for 132 (left side) and 134 (right side). We see that the Z-splitting corresponding to the spherical ^{134}Te dominates in all the three cases, because, as we mentioned earlier its light partner has a sensitive quadrupole deformation and a nonvanishing hexadecupole one. Its Z partner ^{134}Sn has a smaller hexadecupole deformation. The same reasoning apply to A_2=136. Therefore it could be possible that in the case of these nuclei the deformation dictates the yield magnitude rather than the magic number in protons or neutrons. The experimental determination of the double fine structure in this region will, hopefully, clarify the situation.

The *hexadecupole deformed* region, extending from 138 to 156, obtained in the frame of our cluster model, presents also some discrepancies compared to the experimental findings. The main problem that we faced here concerns the odd-even effect which seems to be very strong in this region according to the Tübingen group [29–31]. The things can be understood as follows: In the vicinity of the ground state, the level densities of odd mass nuclei are much larger than for even nuclei and consequently it will be more probable to observe cold fission for odd-odd mass splits in comparison to even-even mass splits. Since in our present calculations the level density of fragments is not taken into account, our results point to an enhancement of even-even mass splits with respect to the odd-odd mass splits. In a preceding paper [32] the effect of level density was incorporated in the calculation of yields by means of the Fermi Back-Shifted Model valid also for small excitation energies. In order to get a rough idea of how the odd-even effect influences the yields, we simply shift the decay energy by the fictitious ground-state position Δ taken from the global analysis of Dilg

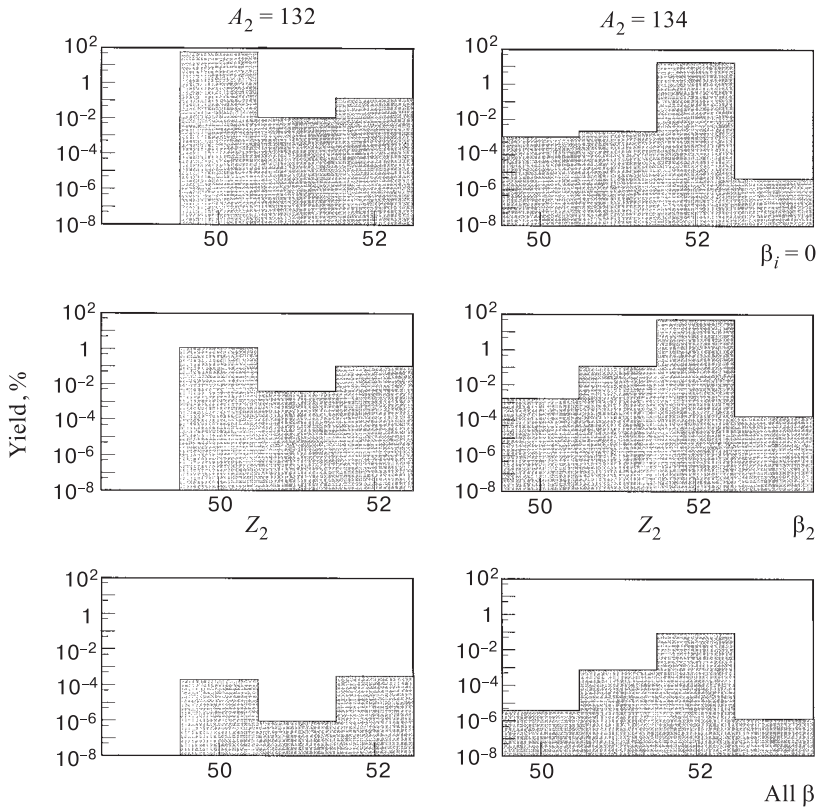

Fig. 10. The yields for the Z splittings of A_H=132, 134 in percents computed with LDM parameters

et al. [33], $Q^* = Q - \Delta$. In Fig.11 we represented the same thing like in Fig.10 but with the above-mentioned shift in the Q value. It is obvious from the inspection of this figure that the odd splittings are enhanced. It is worthwile to stress once again that in our view, in the mass region extending from 138 to 156, the hexadecupole deformation is the leading mechanism responsible for the cold fragmentation of ^{252}Cf. The lowering of the barriers due to hexadecupole deformation increase dramatically the penetrabilities and eventually the yields.

In Fig. 12 we represented the yields for the Z-splittings of A_2=143. Comparing the first two cases we see that the yields are almost unsensitive to quadrupole deformation. When the hexadecupole deformation is included, the distribution changes all the yields being increased almost uniformly (in the log scale). It is worthwhile to notice that the octupole deformations are not inducing the tremendous changes that the hexadecupole do.

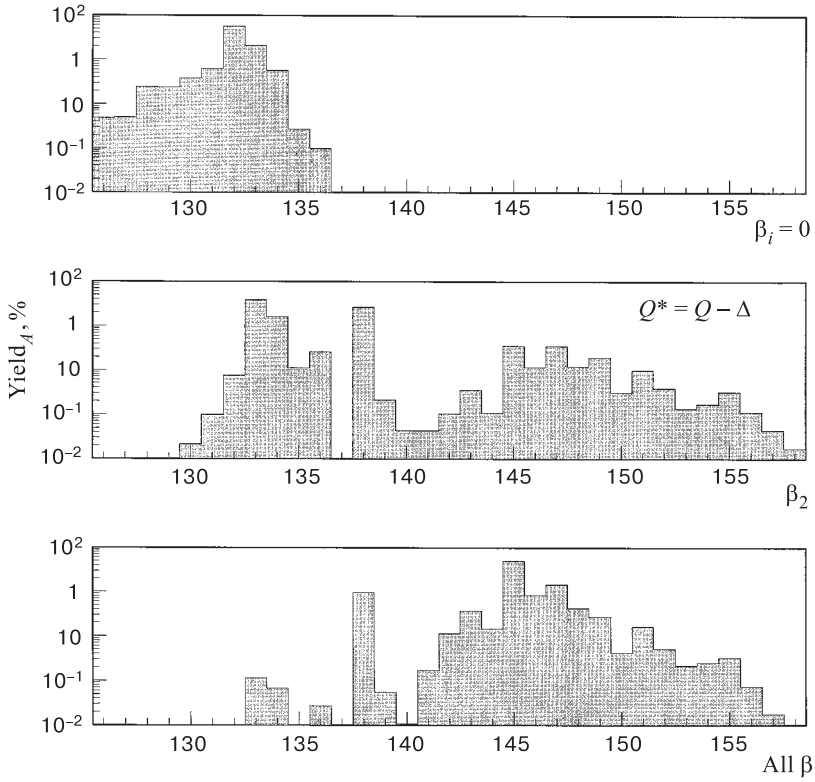

Fig. 11. The mass yields $Y_{A_H} = \sum_{Z_H} Y(A_H, Z_H)$ in percents, as a function of heavy fragment mass computed with LDM parameters with the decay energy modified $Q^* = Q - \Delta$. The odd-odd mass splittings are this time favoured

The main result obtained through these calculations is the theoretical confirmation of the existence of two distinct regions of ^{252}Cf cold fission. The results indicate two different mechanisms. In the heavy mass region situated between 138 and 156, the hexadecupole deformation gives rise to a large number of splittings. Here the shell closure in neutrons or protons seems to not be involved. Although the shell effects should play an important role in the odd-even differences by enhancing the odd-odd mass splits with respect to the even-even ones, our result comfirms that the fragments are emitted with very compact shapes. We should discard deformations much larger than those calculated for the ground state. For such deformations a large part of the excitation energy should be allocated for deforming the fragments. It is not the case for the cold fission system, where one encounters an acute absence of excitation energy. In the spherical region our

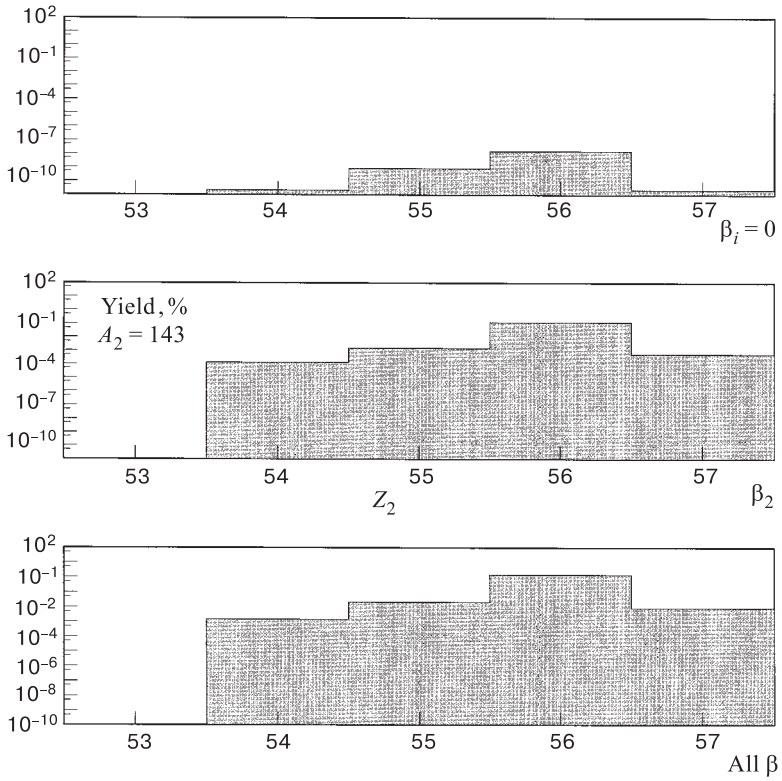

Fig. 12. The yields for the Z splittings of A_H=143 in percents computed with LDM parameters. Calculations without deformations and with the inclusion of quadrupole deformation give nearly the same yields. The inclusion of hexadecupole deformation increases uniformly by 4 orders of magnitude the yields

results give only a hint of the importance of the magic nucleus ^{132}Sn which is susceptible to be produced in a heavy clusterization process, similar to that for light clusters [1]. Here the decay mechanism should be similar to the light cluster radioactivity, the daughter nucleus ^{132}Sn being traded for ^{208}Pb and the heavy cluster ^{120}Cd for ^{32}Si.

4. THE COLD TERNARY FISSION

A. The α-Accompanied Ternary Fission. The first direct evidence of cold (neutronless) alpha ternary fission yields was reported in [17]. Using the triple gamma coincidence technique, only the correlations between the two heavier

fragments were observed unambigously. This new phenomenon is equivalent to cluster radioactivity during fission. Such cold ternary decays produce all the three fragments with very low or zero internal excitation energy and consequently with very high kinetic energies. Their TKE will be close to the corresponding ternary decay energy Q_t. In order to achieve such large TKE values the three final fragments should have very compact shapes at the scission point and deformations close to those of their ground states, similarly to the case of cold binary fragmentations [34].

Below, we develope a coplanar three-body cluster model consisting of two deformed fragments and a spherical α particle for the description of cold (neutronless) alpha accompanied fission of ^{252}Cf. This model is an extension of the cluster model used for the description of cold binary fission that we presented in the preceding section.

In what follows, we apply a semiclassical approach to the tunneling process in a many body system. The system consists in n bodies interacting via a potential $V(\{q_i\})$ which is the sum of two-body components. This assumption is not very restrictive and may be relaxed. Let $\{q_i\}$ be a set of N generalised coordinates. The total available energy for the system is identified with the decay energy Q. We assume that in the classically forbidden region ($V \geq Q$) the usual WKB conditions are fulfiled and the semiclassical many body wave function is given by

$$\Psi \propto exp(-S_0/\hbar), \tag{21}$$

where S_0 is the reduced action between the entrance point and the current point [35]. The action satisfies the Hamilton-Jacobi equations. Consequently the equations of motion (in imaginary time) are the (modified) Euler-Lagrange equations. For a Lagrangian

$$\mathcal{L} = \frac{1}{2}\sum_{i,j=1}^{N} a_{ij}\dot{q}_i\dot{q}_j - V(\{q\}) \tag{22}$$

the reduced action may be written

$$S_0 = \int \sqrt{2(V-Q)\sum a_{ij}dq_i dq_j} \tag{23}$$

and the trajectory is obtained by extremizing S_0 with respect to all possible paths in the coordinates q_i. Parametrizing the path by one of the coordinates, say q_1, we obtain a set of coupled equations:

$$\frac{\partial V}{\partial q_i} = \frac{1}{M}b_i\left(V' + \sum_k \frac{\partial V}{\partial q_k}q'_k\right) +$$

$$+\frac{2}{M}(Q-V)\left(\frac{1}{M}b_i\left(\sum_k a_{1k}q_k'' + \sum_{kl} a_{kl}q_k'q_l''\right) - \sum_k a_{ik}q_k''\right), \qquad (24)$$

where $i,k,l = 2 \div N$ and $f' = \partial f/\partial q_1$. The quantity b_i is defined by

$$b_i = a_{1i} + \sum_k a_{ik}q_k'$$

and the effective mass of the system by

$$M = a_{11} + 2\sum_i a_{1i}q_i' + \sum_{ik} a_{ik}q_i'q_k' \quad . \qquad (25)$$

To the first order of the WKB approximation, the penetrability is given by the square of the wave function (21) with the reduced action calculated on the path satisfying (24) and the boundary conditions

$$V(\{q_{in,out}\}) = Q. \qquad (26)$$

In the particular case $N = 1$ this condition uniquely determines the penetration path. In the general case, the condition (26) does not specify all the necessary conditions for integrating (24). In principle we should solve (24) for all solutions satisfying (26) and choose the path $q_i(q_1)$ which minimizes the reduced action

$$S_0 = \int_{in}^{out} \sqrt{2M(V-Q)}\, dq_1, \qquad (27)$$

where

$$M = M(q_i(q_1), q_1), \qquad V = V(q_i(q_1), q_1) \quad . \qquad (28)$$

This will give the upper bound for the penetrability. In the particular case of a diagonal mass tensor $a_{ik} = \mu_i\delta_{ik}$, Eq.(24) gets a much simpler form:

$$M\frac{\partial V}{\partial q_i} = \mu_i q_i'\left(V' + \sum_k \frac{\partial V}{\partial q_k}q_k'\right) + 2\mu_i(Q-V)\left(\frac{q_i'}{M}\sum_k \mu_k q_k'q_k'' - q_i''\right) \qquad (29)$$

and the effective mass reduces to

$$M = \mu_1 + \sum_k \mu_k (q_k')^2 \quad . \qquad (30)$$

We stress that the system of Eqs. $(26) - (30)$ does not represent a trivial generalisation of the tunneling problem in one dimension. The main difference stems from the fact that Eq.(26) has in general many solutions and the integration of the highly nonlinear coupled equations (29) cannot be started without imposing additional constraints on physical trajectories.

To fix the ideas, let us discuss in some detail the specific features of the tunneling process in the case of cold alpha-accompanied ternary fission. We assume that all three fragments are preexisting in a quasi-bound molecular state. Since the process is cold, the heavy fragments have very compact shapes with deformations close to their asymptotic values. Strong polarisation effects are expected in the initial stages of the tunneling process. One may include such effects by introducing effective deformations. In order to grasp the penetrabilities for the most probable processes one may consider only axial deformations with symmetry axis oriented along the fission axis. For simplicity the problem is reduced to a planar one and therefore we have to deal with six coordinates. Requiring the c.m. to be at rest, we are left with four independent coordinates. Let $(x_i, y_i,\ i = 1, 2)$ be the fragment coordinates and (x_α, y_α) the coordinates for the α particle. The corresponding masses are denoted by $m_i,\ i = 1, 2, \alpha$. The usual transformation to relative coordinates $R = x_2 - x_1$ and $y = y_2 - y_1$ leads to

$$x_1 = \frac{-m_\alpha x_\alpha - m_2 R}{m_1 + m_2} \quad , \quad y_1 = \frac{-m_\alpha y_\alpha - m_2 y}{m_1 + m_2},$$

$$x_2 = \frac{-m_\alpha x_\alpha + m_1 R}{m_1 + m_2} \quad , \quad y_2 = \frac{-m_\alpha y_\alpha + m_1 y}{m_1 + m_2}.$$

The kinetic energy and the third component of the angular momentum in terms of these coordinates are

$$T = \frac{1}{2}\left(\mu_{12}(\dot{R}^2 + \dot{y}^2) + \mu_\alpha(\dot{x}_\alpha^2 + \dot{y}_\alpha^2)\right), \tag{31}$$

$$L_z = \mu_{12}(R\dot{y} - \dot{R}y) + \mu_\alpha(x_\alpha \dot{y}_\alpha - \dot{x}_\alpha y_\alpha), \tag{32}$$

where

$$\mu_{12} = \frac{m_1 m_2}{m_1 + m_2}, \qquad \mu_\alpha = m_\alpha\left(1 + \frac{m_\alpha}{m_1 + m_2}\right).$$

Since the α-particle mass is small compared to the fragment masses, we further assume $y \approx 0$ on the penetration path. This assumption may lead to a nonconservation of the angular momentum (32). However, we expect a very smooth α-particle trajectory, and to a good approximation the second term in (32) is vanishingly small. Next, requiring $L_z = 0$ implies $y \simeq const.R$. In the initial configuration one can always choose the heavy fragments along the x axis and therefore $const = 0$ and the angular momentum is conserved. Similar considerations lead to the conclusion that even the kinetic energy (31) is well evaluated along the trajectory. Since $y \approx 0$ seems to be a reasonable approximation, one further assumes $y_1 \approx y_2 \approx 0$.

We are finally left with the problem of finding the α-particle coordinates (x_α, y_α) as a function of the interfragment distance R, which is a natural candidate

for the variable q_1. A close inspection of Eq.(31) readily identifies the necessary mass parameters and the action integral reads:

$$S_0 = \int_{R_{in}}^{R_{out}} \sqrt{2\left\{\mu_{12} + \mu_\alpha \left(\left(\frac{\partial x_\alpha}{\partial R}\right)^2 + \left(\frac{\partial y_\alpha}{\partial R}\right)^2\right)\right\}(V - Q_t)}dR \qquad (33)$$

with $V = V\left(x_\alpha(R), y_\alpha(R), R\right)$. The above formula shows that under well justified approximations the penetrability for the three-body system is similar to the well-known WKB expression for two body systems with an important correction in the effective mass arising from the α-particle trajectory. The one dimensional case is reproduced in the limit $\mu_\alpha \to 0$. The magnitude of this correction can be determined by solving the nonlinear coupled equations (29). Subsequent numerical calculations with selected trajectories showed that the most important contribution arises from the variation of y_α with the interfragment distance.

The total interaction potential is obtained as the sum of two-body potentials between the α particle and the fragments and between the light and heavy fragment. An advantage of this approach is that the barrier between the two fragments and the barrier between the α particle and the fragments can be calculated quite accurately due to the fact that the touching configurations are situated inside the barriers. An important requirement for the interaction potential is that the system should enter the penetration path very close or beyond the touching configuration. This point will be checked carefully in the following.

The data base for the present calculation includes 78 different splittings for alpha ternary fission and 87 splittings for binary fission of ^{252}Cf. Each splitting is defined by charge and mass numbers, experimental binary and ternary decay energies and a set of geometrical and deformation parameters which characterize the one-body densities.

In order to understand the landscape of the three-body potential we first represent the potential at different interfragment distances R (Fig.13) with heavy fragments in a nose-to-nose configuration, for the splitting ^{4}He +^{92}Kr+^{156}Nd with deformed fragments. The potential for a splitting with a spherical fragment looks quite similar. In the equatorial plane we distinguish a saddle configuration which results from the interplay of the strong repulsive (Coulomb) forces acting on the α particle and the attractive (nuclear) forces. The saddle trajectory is obtained by numerically solving the equation

$$\frac{\partial V}{\partial x_\alpha} = 0$$

for fixed interfragment distance. Along the saddle trajectory there are two interesting extrema: one is situated on the symmetry axis and another one at the top of

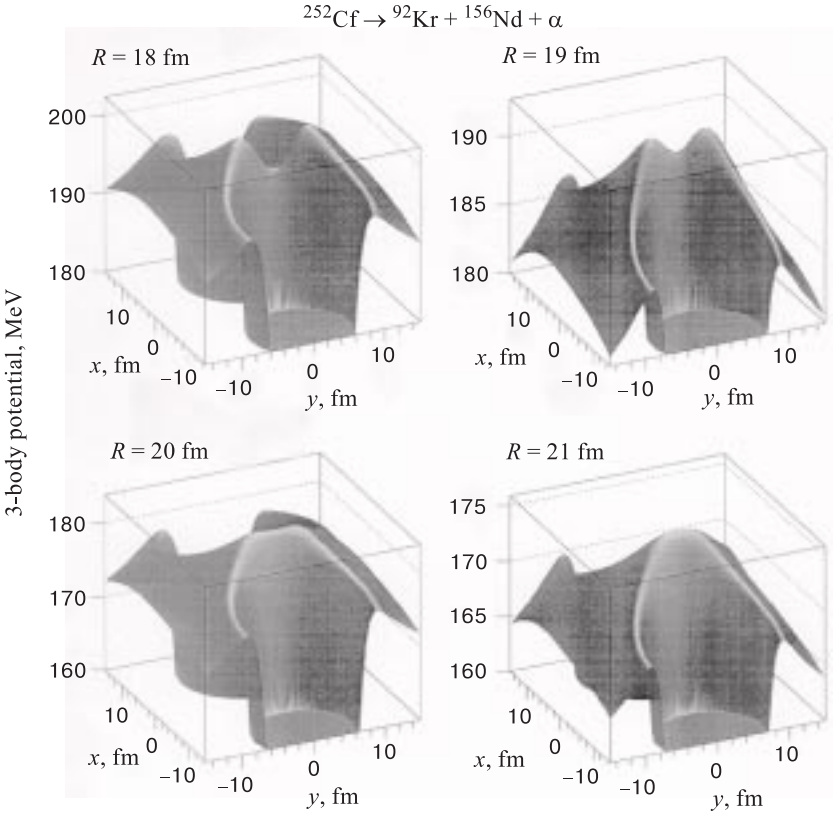

Fig. 13. The three-dimensional ternary potentials for the splitting ^{4}He+^{92}Kr+^{156}Nd at different interfragment distances $R = 14, 15, 16, 17$ fm between the colinear fragments in a nose-to-nose configuration. We can see the two wells corresponding to the light and heavy fragment and in the equatorial plane a ridge which grows up with the interfragment distance R between fragments. This ridge has a minimum on the symmetry axis and a maximum at the equatorial alpha barrier height. This minimum disappears at large interfragment distances $R \simeq 20 - 21$ fm

the maximum of the equatorial alpha barrier ridge where all classical forces acting on the α particle are equilibrated. This last point is denoted in the following as the Lagrange point and the ensemble of such points for different interfragment distances — the Lagrange trajectory. As can be seen in Fig.13 the minimum situated on the symmetry axis disappears at large interfragment distances $R = 20 - 21$ fm. Following Radi et al. [36], we assume that the position of the α particle is governed by the well the potential has in the perpendicular direction. If the motion is not very fast, the α should adiabatically adjust to a stationary state in this

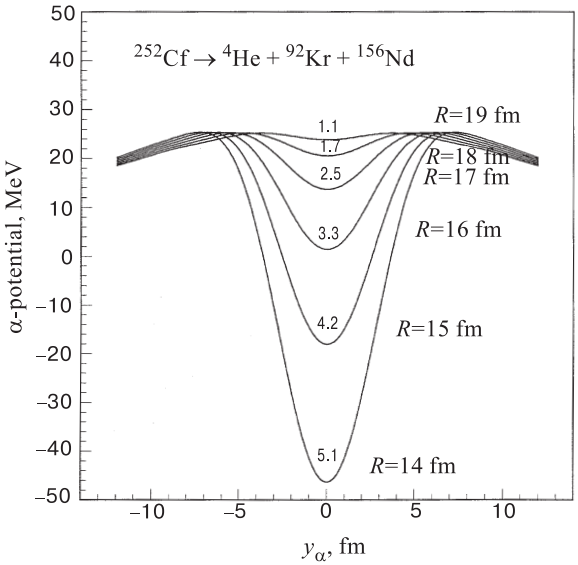

Fig. 14. The ternary potential minimum in the equatorial plane for the splitting ^{4}He+^{92}Kr+^{156}Nd at different interfragment distances R. The corresponding zero point energies in an harmonic oscillator approximation are indicated. As can be seen at large R this minimum disappears

potential. To get the position of the α particle we approximate this potential with an harmonic oscillator potential

$$V(y) = V_{min} + \frac{1}{2}Cy^2, \tag{34}$$

where the stiffness coefficient C depends on the interfragment distance and is obtained by numerically differentiating the potential around the minimum. Then the eigenvalues are given by:

$$E_n = \left(n + \frac{1}{2}\right)\hbar\sqrt{\frac{C}{m_\alpha}}. \tag{35}$$

A convenient measure of the spread of this position is given by:

$$< y^2 >_n = \frac{E_n}{C}. \tag{36}$$

In Fig.14 the saddle potential and the zero point energies are represented as a function of R for the splitting ^{4}He+^{92}Kr+^{156}Nd with deformed fragments. The

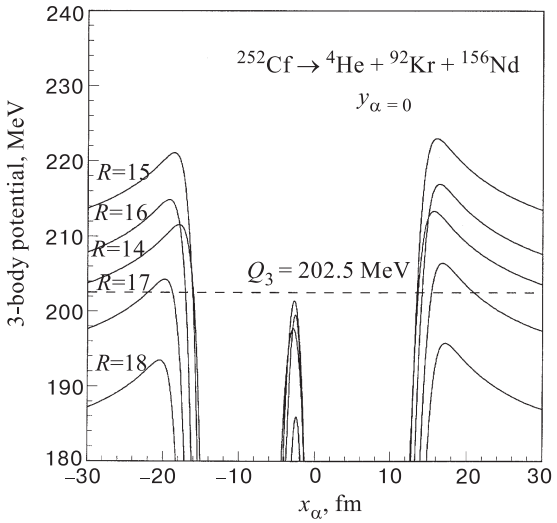

Fig. 15. The ternary potentials $V(x_\alpha, y_\alpha = 0, R)$ for the splitting ^{4}He+^{92}Kr+^{156}Nd as a function of x_α for different interfragment distances R. The two wells and the two polar barriers corresponding to the light and heavy fragment are clearly seen. At $R > 17$ fm the polar barriers are below the ternary Q_3 value. The interfragment ridge situated in the equatorial plane is very narrow

zero point energies are consistent with the previous estimation of Radi et al. [36]. In Fig.15 we represented, for the same splitting at different interfragment distances R, the polar alpha barriers, i.e., the potential $V(x_\alpha, y_\alpha = 0, R)$. We can clearly see the two wells corresponding to the light and heavy fragments which are separated by a very narrow interfragment ridge. Also we can see that the polar barriers disappear at the interfragment distance $R \simeq 17$ fm that is much earlier than the equatorial barriers. We must stress that the semiclassical approximation for the penetration factor requires the penetration path be localized in a region, where $V \geq Q_t$. This is the most economic way to localize the position of α particle during the penetration path in the present model. In Figs.16a and 16b, for the above splitting with deformed fragments and the splitting ^{4}He+^{117}Pd+^{131}Sn with a spherical fragment, we represented the three-body potential $V(x_\alpha, y_\alpha, R)$ in the plane (x_α, y_α) at different interfragment distances by only one equipotential line Q_t. At small interfragment distances the uncertainty in the α particle position is rather large but it reduces drastically as R increases. We can see that by increasing R the Q_t-value contours are reduced practically to a single point. One remarks also that at the exit points the y coordinate of the α particle has the rather large values, of the order of 5 fm for two deformed fragments and slightly larger (6 fm) when one fragment is spherical. Such high values, are consistent with

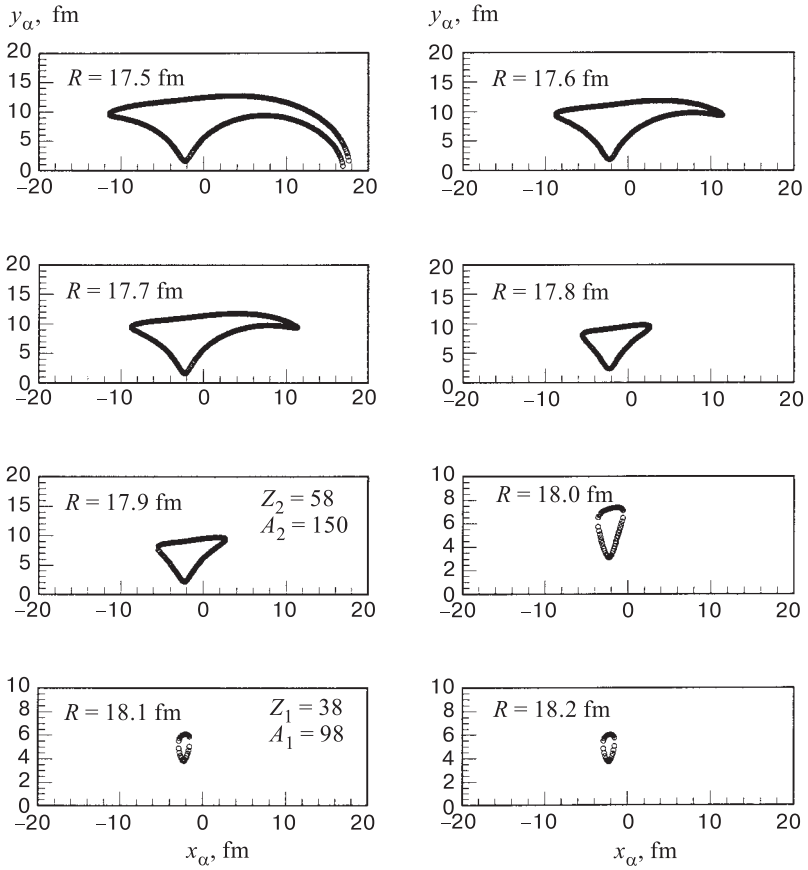

Fig. 16. The ternary potentials $V(x_\alpha, y_\alpha, R)$ represented in the plane (x_α, y_α) by a single equipotential line Q_t at different interfragment distances R for the splittings: a) ^{4}He+^{92}Kr+^{156}Nd with deformed fragments and b) ^{4}He+^{117}Pd+^{131}Sn with a spherical heavy fragment. At large R the exit points are quite different for such splittings. This suggests different energy and angular distributions of the α particle for the two regions

Eq.(36) only if the α particle is placed in a rather high excited state in the saddle potential. Also one can remark that the penetration path terminates much earlier in the case of one spherical fragment as compared to the deformed-deformed case. Based on this observation one may conjecture that the angular and energy distributions of the α particle which are largely determined by the configuration at the end of the penetration path will be rather different in the two cases.

Other possible characteristics of the three-body potential are given in Figs.17a and 17b. Here we represented in the plane (x_α, y_α) for the above two splittings

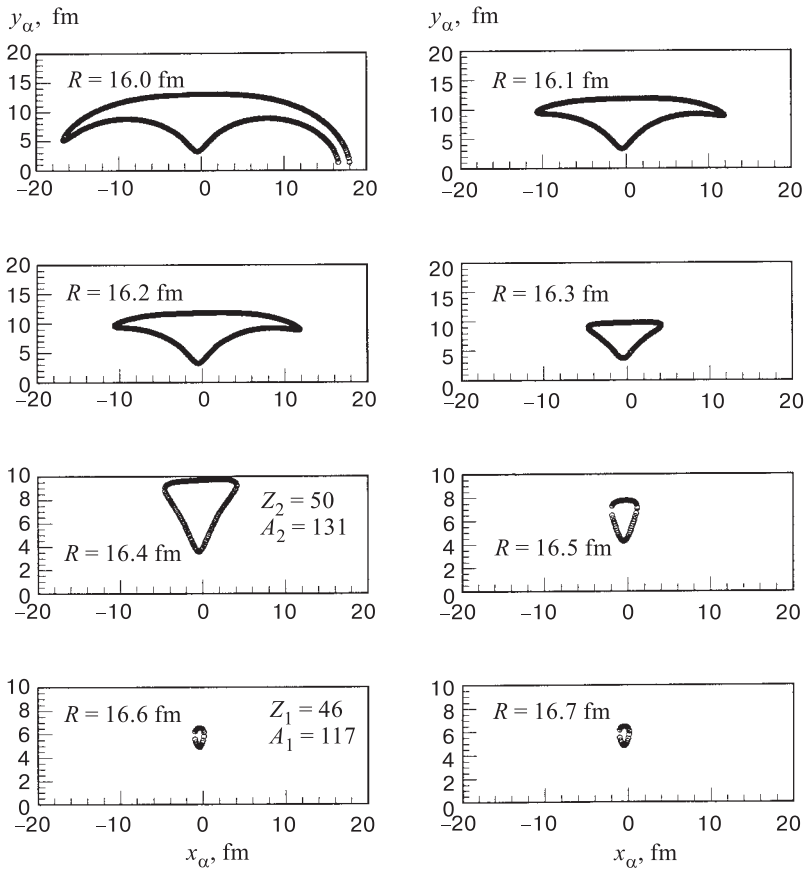

Fig. 16*b*

the fragments with all deformations included and the two ridges: the equatorial one defined by the equilibrium of the classical forces acting on the α particle in the x direction and the α particle ridge defined by the top of the α barriers situated around the two fragments. The intersection of these two ridges gives the Lagrange point where no forces are acting on the α particle. We also represented the centres of the α particle obtained from the geometrical condition that the α particle is in touch with each fragment. We define a touching point such that the densities of the two bodies in contact are half of their central value. We see that the intersection of the two touching configurations of the α particle and the two fragments is not situated on the equatorial ridge. Due to the fact that this ridge is very narrow (see Fig.15) we have to impose the condition that the α

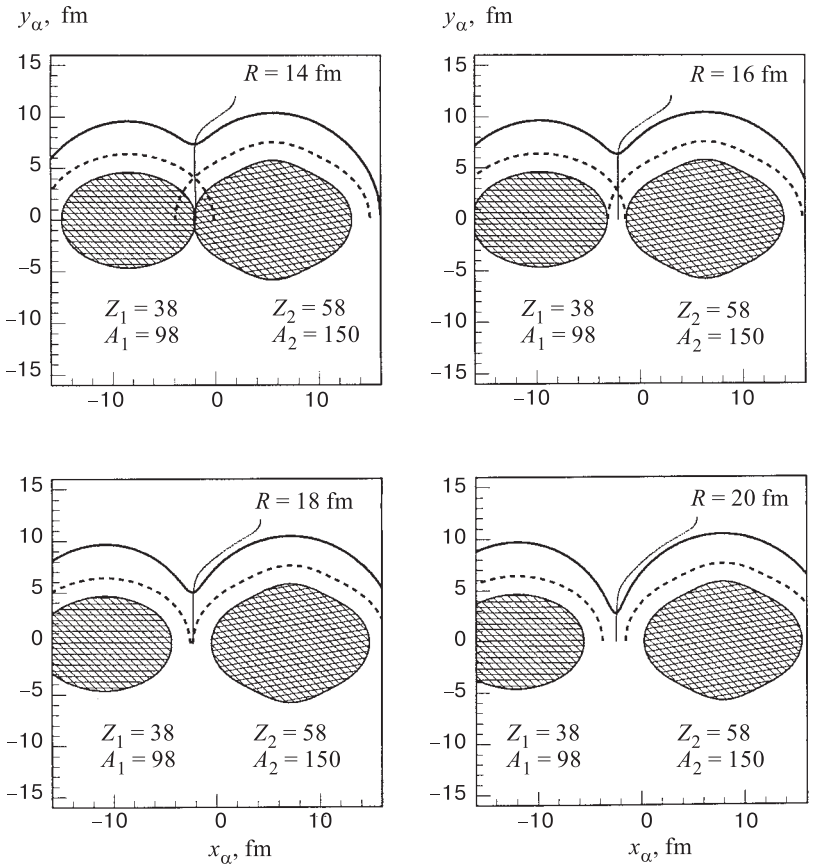

Fig. 17. Schematic representation of the two fragments for the splittings mentioned in Fig. 16. The fragment shape is defined by the the half-density surface. The dashed line represents the locus of the centre of the α particle in touching with one of the fragment. The thick continous line represents the α particle ridge while the thin line is the equatorial ridge. The intersection of the two continous lines gives the Lagrange point (see text for details)

particle is in equilibrium on the ridge, in order to exclude the cases of subsequent disolution of the α particle in one of the fragments. This condition together with the touching condition with one of the fragments defines the adiabatic trajectory when the interfragment distance is varied. We recall here that the Lagrange trajectory which explores the maximal values of the interaction potential gives a lower bound of the penetrability while the more physically intuitive adiabatic trajectory gives an upper bound.

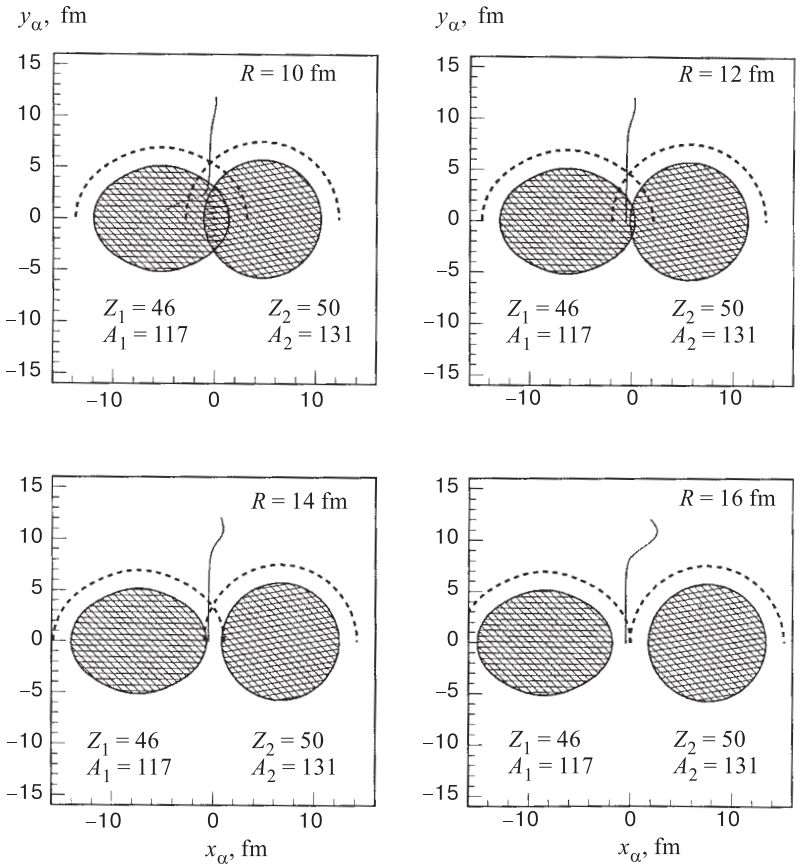

Fig. 17*b*

One possible physical choice of the α particle initial position is situated on the interfragment ridge and above the touching curves as previously defined. On the other hand, if we allow the α particle to overlap the fragments, we can consider different scenarios which could be related to the excited quantum states defined in the equatorial ridge well.

In our static description of the alpha accompanied fission, the alpha ternary yields depend essentially on the α particle trajectory. This limits considerably the number of possible scenarios. In the following we shall consider only few scenarios.

The *first* one is the *adiabatic scenario*. This assumes that the α particle is situated on the interfragment ridge, satisfying one of the two α particle touching configurations, i.e., at the lowest y_α^0 value. By increasing the interfragment

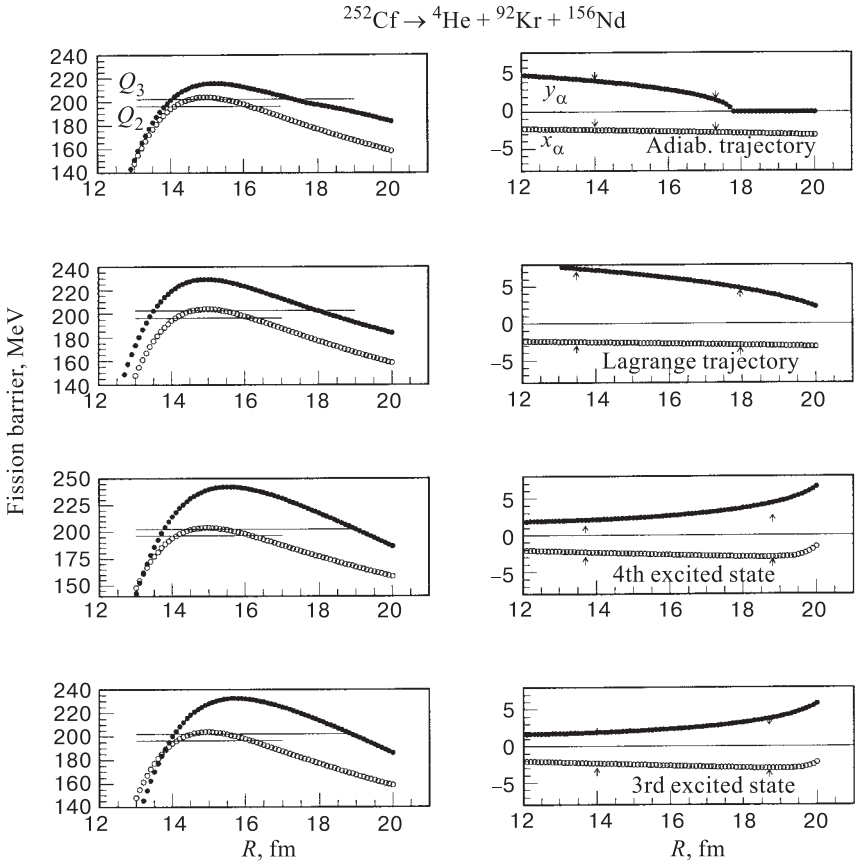

Fig. 18. Fission barriers and α-particle trajectories for the splittings mentioned in Fig. 16. Left panels: ternary barriers calculated along selected trajectories and binary barriers for the cold fission of the daughter nucleus ^{248}Cm leading to the same fragments. The corresponding ternary and binary reaction energies are indicated by thin lines. Right panels: The α-particle trajectories (x_α, y_α) versus the interfragment distance R. The inner and outer turning points are indicated by arrows

distance R, the α particle is getting closer to the fragment symmetry axis. The corresponding α particle trajectory together with the ternary and binary barriers are plotted in Figs.18 for the above two splittings: a)^{4}He+^{92}Kr+^{156}Nd and b) ^{4}He+^{117}Pd+^{131}Sn. Also we represented the intersection of the barriers with the Q values, i.e., the corresponding inner and outer turning points. Note that the system crosses the ternary barrier before the α particle becomes colinear with the fragments.

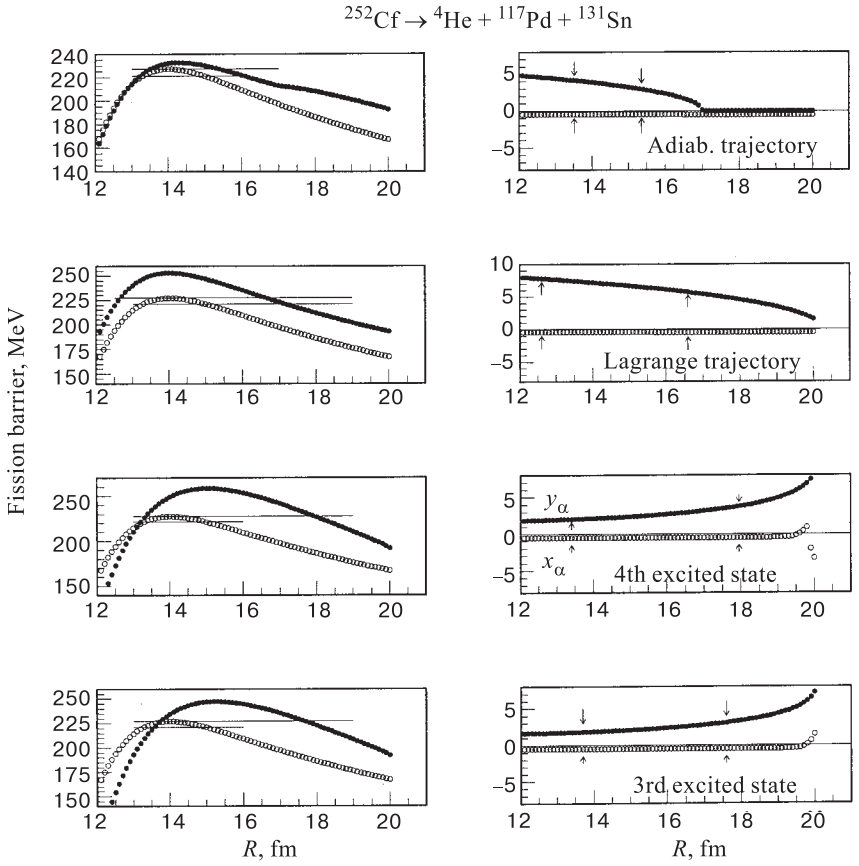

Fig. 18*b*

The *second* scenario is the *Lagrange scenario*. In this case we assume that the α particle is situated at the Lagrange point were all forces acting on the α particle are in equilibrium. The α particle trajectories and the corresponding barriers are represented also in Figs.18. Also we plotted the binary barriers of ^{248}Cm for the same splittings. Clearly the ternary barrier is higher than the binary one and shifted to larger R distances. As previously discussed the α particle motion in the transversal well is taken into account by substracting from the Q_t value its energy (35). This procedure does not provide for a ternary barrier the Q_t value when considering the ground and first two excited states. Therefore we consider only the third and fourth excited states *scenarios*. In the same Figs.18, the α particle trajectories and the corresponding ternary barriers for the third and fourth excited states are represented by including the $E_n(R)$ values in the barriers.

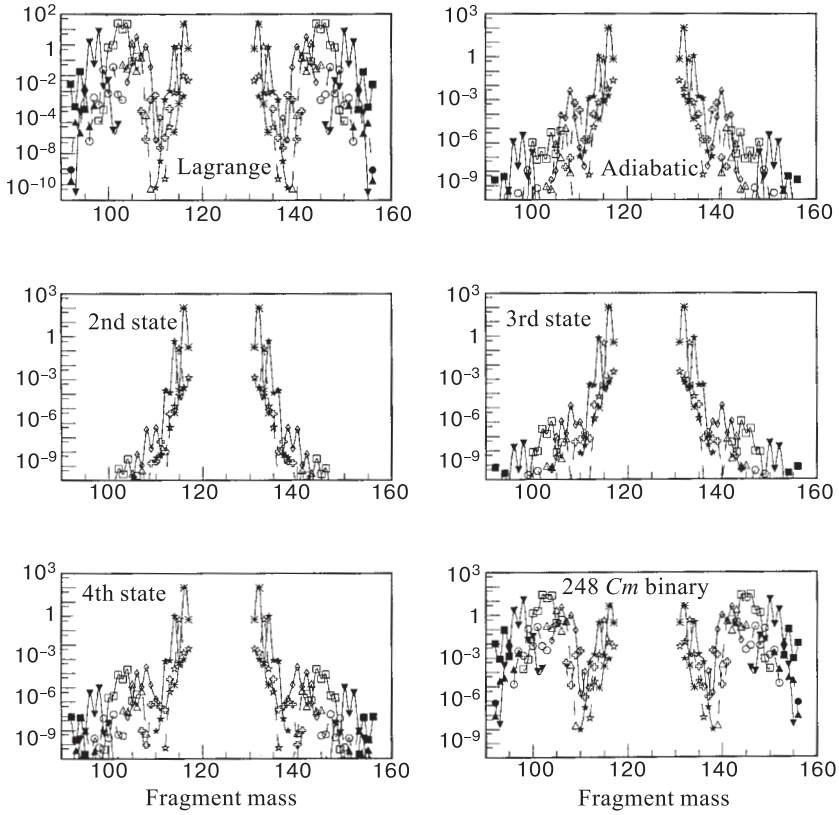

Fig. 19. The cold alpha ternary yields of ^{252}Cf for the Lagrange, adiabatic, second, third, and fourth state scenarios, corresponding to different initial positions of the alpha particle on the interfragment ridge, as a function of fragment mass. Also the cold binary yields of ^{248}Cm are given. With the exception of ternary yields obtained in the Lagrange scenario, which are very similar with the cold binary yields of ^{248}Cm, all scenarios strongly favour the splitting ^{4}He+^{116}Pd+^{132}Sn with one spherical fragment

Obviously, for these scenarios the y_α^0 initial values of Eq.(36) are smaller than for the Lagrange configuration, which assumes the maximum y_α^0 values at the top of the α barriers, and even smaller than the values for the adiabatic scenario which is based on the lowest energy configuration.

Knowing the barriers and Q_t values, the relative alpha ternary yields are given by the same formula like in the binary case (see Eq.(20)).

The preformation factors for an α particle at the surface of a deformed fragment differs by orders of magnitude as compared to the spherical case. Nevertheless, in this case, like in the binary case, no preformation factors are considered.

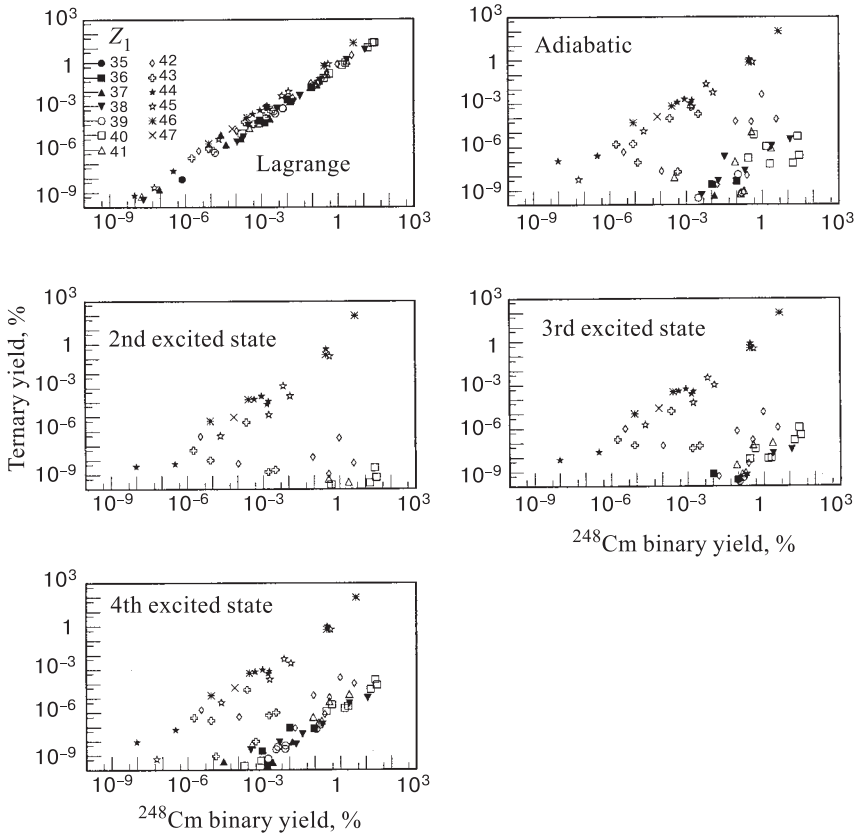

Fig. 20. Scatter diagram of the cold alpha ternary yields of ^{252}Cf for Lagrange, adiabatic, second, third, and fourth state scenarios versus the cold binary yields of ^{248}Cm. Only the ternary yields of ^{252}Cf obtained in the Lagrange scenario are strongly correlated with the cold binary yields of the daughter nucleus ^{248}Cm. For all other possible scenarios only the splitting with ^{132}Sn is favoured

Once again, as fragment deformations we choose the ground state deformations computed in the framework of the macroscopic-microscopic model. These deformations play a very important role on barrier penetrabilities, i.e., on ternary yields. The light fragments have mainly quadrupole deformations in contrast to heavy fragments which have all kinds of deformations. The octupole deformations exist for a small heavy fragment mass region $141 \leq A_H \leq 148$. The fragments with mass numbers $A_L < 92$ and $A_H < 138$ are practically spherical. In the following we shall include all deformation up to $\lambda = 4$ with positive values, i.e., oblate shapes ($\beta_2 < 0$) are transformed to prolate shapes ($\beta_2 > 0$) and neck shapes ($\beta_4 < 0$) to shapes with positive hexadecupole deformations ($\beta_4 > 0$).

The ternary fission yields for different scenarios: Lagrange, adiabatic, second, third and fourth excited states, corresponding to different initial positions of the α particle on the interfragment ridge are represented in Fig.19. Also the cold binary yields for ^{248}Cm are given. With the exception of the Lagrange scenario yields, which are very similar to the cold binary yields of ^{248}Cm, all other scenarios are strongly favouring only the spherical splittings.

In Fig.20, for the same scenarios, the ternary yields versus binary yields of the daughter nucleus ^{248}Cm leading to the same splittings are displayed. Only in the Lagrange scenario the alpha ternary yields are strongly correlated with the cold binary yields of the daughter nucleus. Such a possibility is consistent to the fact that binary barriers are very thin (with only 2–3 fm width) [34]. For the other scenarios, adiabatic, second, third and fourth excited states, only the ternary yields for spherical splittings, which are dominated by the Q-value principle become important. This fact is not consistent with the existing experimental data on cold alpha ternary yields [17], which indicate cold alpha ternary yields for both regions.

B. Observation of ^{10}Be Emission in the Cold Ternary Fission. Preliminary data for the cold (neutronless) ^{10}Be-accompanied and ^{14}C- accompanied ternary fragmentations of ^{252}Cf were obtained [37, 38] using the Gammasphere with 72 Compton suppressed Ge detectors.

Contrary to α-ternary fission whose first excited state is located very high in energy (>20 MeV), ^{10}Be has an excited state (2^+) at an energy of 3.368 MeV. Therefore we cannot expect cold fission to the first excited state of the α particle. Instead, ^{10}Be and other heavier ternary fragments are more easily polarizable and thus collective effects can be enhanced. The possible excitation of relative vibrations and rotation modes of the three fragments will alter significatively the angular distribution of the emitted fragments.

In order to detect directly ^{10}Be, two complementary partners, ^{96}Sr and ^{146}Ba, were chosen, which are situated near the peaks of the mass distribution of ^{252}Cf. Clearly the missing third particle is ^{10}Be [39]. The coincidence spectrum was obtained by gating on the $2^+ \rightarrow 0^+$ transition of energy 181.1 keV in ^{146}Ba and on the $4^+ \rightarrow 2^+$ transition of energy 977.5 keV in ^{96}Sr. The transitions $4^+ \rightarrow 2^+$, with energy 332.6 keV, in ^{146}Ba and $2^+ \rightarrow 0^+$ with energy 814.7keV in ^{96}Sr, were clearly observed [39].

Further, it was checked that the missing third fragment is really ^{10}Be. Examining the high energy region of the same coincidence spectrum, a peak with energy 3368 KeV was observed and assigned to the $2^+ \rightarrow 0^+$ transition in ^{10}Be.

Recently, the Darmstadt group [40] reported evidence that ^{10}Be nuclei, in a rather high excited state of 3.37 MeV, are produced in ternary fission. A puzzling fact was that a part of the γ quanta with this energy are apparently emitted from rest. Since the flight time of Be nuclei to the detector($\approx$ 2ns) is much longer than the lifetime of the 3.37 MeV level (180 fs), we face a huge delay in the

emission of the ternary particle, if we suppose that the emission takes place in the detector. In other words the γ quanta seems to be emitted rather from a quasi-bound *trinuclear* state, which has a lifetime much larger than the estimated time of acceleration in the Coulomb field of the fissioning system. This possible quasi-bound state arises in the potential pocket produced by the mutual interaction of the three fragments.

C. Trajectory Calculations for the Alpha-Accompanied Ternary Cold Fission. In order to get a hint on the configuration and the dynamics of the fissioning nucleus at scission a large number of studies were devoted in the past to the trajectory calculation, specially for α particles emitted from the neck region [41–46]. The authors who considered the finite size and the deformation effects [36,47,48] showed that these geometrical factors are influencing sensitively the angular distributions of the α particle.

Making a good selection for the initial parameters of the trajectory calculations is a difficult task. This is due to the fact that probing various combinations of assumed initial conditions and then computing the trajectories for comparison with the available experimental data, similar results are often obtained. In the hot alpha accompanied ternary fission the initial conditions are taken in various combinations. For example the initial kinetic energy of the two main fragments and of the α emitted in the spontaneous ternary fission should be around 0.5 MeV according to the statistical theory and the equipartition principle [44,45]. On the contrary, in the dynamical theory of fission [49] the nascent fragments at scission are predicted to be moving with appreciable kinetic energy (20–50 MeV).

As we showed in the previous section, for the cold ternary fission the initial conditions are better known. We have to establish the following initial conditions:

a) The Shape of the Fragments. The determination of the shape of the fragments in the ternary cold fission is facilitated, up to a certain extent, by the peculiar characteristic of the process, i.e., the fragments should have very compact shapes at the scission point and deformations close to those of their ground states. One may next suppose that the shapes of the fragments will not be modified when the fragments move away in the Coulomb field of each other.

b) The Tip Distance d. Naturally, d should correspond to the configuration at which the α particle is released. As can be inferred from Fig.13, the light particle should stay between the two heavy fragments in a position which should avoid its absorbtion by any of the fragments. We see in Fig.21, that for tip distances up to 7 fm, the α is facing a thick barrier in the transversal direction. Eventually as the distance between the fragments increases, the pocket in which the α is located becomes more and more shallower until it disappears around d = 8 fm. Therefore one may conclude from these qualitative arguments that the initial tip distance between the two main fragments should not be larger than that corresponding to the disappearence of the pocket.

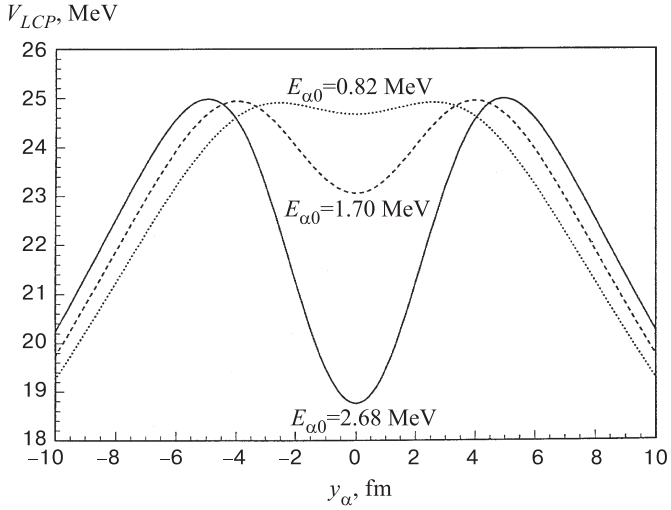

Fig. 21. The one-dimensional potential well of the α particle for three different tip distances: d = 6 fm (full line), d = 7 fm (dashed line), d = 8 fm (dotted line)

c) Initial Geometric Configuration of the α Particle. We invoke a receipt proposed by Boneh et al. [42] considering as a possible choice for the α position, the point of minimum potential energy (the saddle point of the potential energy surface) that we mentioned in the first section of this chapter. In the case of our deformation-dependent cluster model, where the nuclear forces are introduced via the M3Y potential, this saddle point corresponds to the position where the combined Coulomb and nuclear forces exerted by the heavy fragments on the α particle cancel each other, and the potential surface will have a relative minima at this point. The method by which this point is determined was explained earlier so we will not return to it.

d) The Kinetic Energy of the α Particle E^0_α. As we already noted above the potential energy of the α positioned at the electro-nuclear saddle point will have a minimum in the y direction. It is clear that the α particle has no component of its velocity along the x axis since this would result in a possible absorbtion by the deep potential wells of the two heavier fragments instead of being emitted(see Fig.13). The only chance for the α particle to not be reabsorbed during the descent of the decaying system from scission to the release point is to have a momenta directed only along the y axis. Taking sections of the potential surface along the y axis at x corresponding to the saddle point, the resulting potential slice will look similar to a one-dimensional harmonic potential well (see Figs. 14 or 21). When the tip distance increases, the well becomes more and more shallow until it vanishes completely. Using the ideas outlined in the first subsection

of this chapter we approximate the potential V_α with an harmonic potential in the y direction, centered at the saddle-point(see Eq.(34)), and eventually get an estimation for the initial kinetic energy of the α supposing that it can be identified with the zero-energy in this *harmonic* potential well, i.e.,

$$E_\alpha = \frac{1}{2}\hbar\sqrt{\frac{C}{m_\alpha}}, \tag{37}$$

where the stiffness constant is given by the expression

$$C = \sum_{i=L,H} \frac{1}{R^0_{\alpha i}} \sum_{\lambda \geq 0} \left(\left. \frac{\partial V_{\lambda 0 \lambda}(R_{\alpha i})}{\partial R_{\alpha i}} \right|_0 - \frac{\lambda(\lambda+1)}{2} \frac{V_{\lambda 0 \lambda}(R^0_{\alpha i})}{R^0_{\alpha i}} \right), \tag{38}$$

where $R^0_{\alpha i}$ is the distance from the fragment i to the α located at the saddle point:

$$R^0_{\alpha L} = \frac{D}{1+\sqrt{\frac{Z_L}{Z_H}}}, \qquad R^0_{\alpha H} = \frac{D}{1+\sqrt{\frac{Z_H}{Z_L}}}, \tag{39}$$

where D is the interfragment distance. For increasing tip distance the kinetic energy of the α decreases. One might suppose that in the range 6–8 fm, for the tip distance, the light particle has the possibility to escape by tunneling or by the disappearance of the barrier. Further the velocity corresponding to this kinetic energy, $v_\alpha = \sqrt{\frac{2E_\alpha}{m_\alpha}}$ will have a nonzero component only with respect to the y axis, according to the above discussion.

e) The Kinetic Energies of the Two Main Fragments E^0_H, E^0_L. Usually in trajectory calculations for the spontaneous fission different choices are taken for the initial kinetic energies of the fragments emitted in the process. The initial velocities of the heavy fragments are considered to have nonzero components only along the x axis. The initial velocity of the light fragment $v_L(0)$ is related to the initial velocity of the heavy fragment $v_H(0)$ in such a way that the total momentum of the two fission fragments is zero along the x axis, i.e., $v_L(0) = \frac{A_H}{A_L} v_H(0)$. Although this assumption violates the conservation of linear momentum, the error introduced is usually negligible. In order to determine the kinetic energies of the two main fragments we make use of the considerations derived from the deformed cluster model that we employed in a previous paper for the study of the ternary cold fission [34]. We strongly rely on the conclusion that we drew earlier and which states the existence of a strong correlation between the cold alpha ternary yields of ^{252}Cf and the cold binary yields of the daughter nucleus ^{248}Cm. For the binary cold fission of ^{248}Cm, the exit point from the potential barrier is at a tip distance d around 3 fm, as can be seen in Fig. 22, for the splitting $^{248}\text{Cm} \rightarrow {}^{104}\text{Mo} + {}^{144}\text{Xe}$. This barrier is much thiner than the barrier between the α particle and the heavier fragments, and thus in our model the first

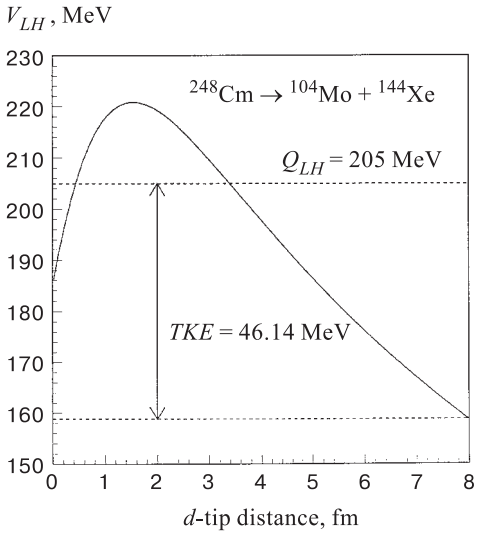

Fig. 22. The barrier between the two heavier fragments

two heavier fragments penetrate the potential barrier between them and later on the light particle is emitted.

On ground of the cold fission characteristics mentioned above one may conjecture that at the exit point (second turning point) of the two heavier fragments, their potential energy is equal to Q_{LH} and their kinetic energy is equal to zero. When the fragments move apart, i.e., their tip distance increases, their kinetic energies increase, too. In order to estimate the total kinetic energy of the fragments we have to find out at which tip distance the release of the α is likely to occur and compute at that point the potential energy, i.e.,

$$TKE(d) \equiv TKE_L + TKE_H = Q_{LH} - V_{LH}(d). \tag{40}$$

Using the conservation of linear momentum invoked above we have

$$TKE_L = \frac{A_H}{A_L} TKE_H \tag{41}$$

and the individual kinetic energies in terms of the total kinetic energy reads

$$TKE_i = \frac{A_j}{A_H + A_L} TKE(d) \quad (i, j = L, H, i \neq j). \tag{42}$$

If we choose d = 8 fm for the splitting considered in Fig.22, then we get for the total kinetic energy of the two main fragments TKE=46.21 MeV which

is much larger than the corresponding kinetic energy in the spontaneous fission. For d = 6 fm the kinetic energy will drop to TKE=28.78 MeV. Repeating this calculation for other mass splittings we conclude that the kinetic energy of the main fragments is ranging in the broad interval 25 — 50 MeV, but as we shall see bellow it is correlated to the kinetic energy of the α through the tip distance.

After determination of the configuration at the release point we have to establish the forces acting between fragments in order to write down the equations of motion. The forces are central, and the initial velocities are confined in the $x-y$ plane. Thus the problem is simplified by a two-dimensional approximation. There will be required six coordinates and six velocities, which are governed by a system of twelve first-order ordinary differential equations. Contrary to other works we take into account the forces exerted by the α on the fragments. We proceed to the calculation of the trajectories by considering only the Coulomb forces. Since the kinetic energies of the fragments are rather high, this approximation is good even in the point-charge approximation.

In what follows we consider that the symmetry axes of the fragments are lying in the same plane. Using the formalism presented in chapter 1, the interaction between two heavy ions with orientation Ω_1, Ω_2 of their intrinsic symmetry axes with respect to the fixed frame, is given by Eq.(4). In the present study the α is spherical and thus the interaction between the α and one heavy fragment i(=L, H) will get a simplified form

$$V(\mathbf{R}_{\alpha i}) = \sum_{\lambda} U^{\ 000}_{\lambda 0 \lambda}(R_{\alpha i}) P_{\lambda}(\cos\theta_{\alpha i}). \tag{43}$$

The following approximation can be applied for the two heavy fragments : Since their relative orientation does not change significantly at the beginning of the quasi-classical motion, one can neglect the relative orientation of the heavy fragments:

$$V(\mathbf{R}_{LH}) = \sum_{\lambda_1 \lambda_2 \lambda_3} U^{\ 0\ 0\ 0}_{\lambda_1 \lambda_2 \lambda_3}(R_{LH}) P_{\lambda_3}(\cos\theta_{LH}). \tag{44}$$

The force acting between a pair of fragments can be written:

$$\mathbf{F}_{ij} = -\nabla V(\mathbf{R}_{ij}). \tag{45}$$

The equations of motion of the three nuclei are:

$$M_L \ddot{\mathbf{r}}_L = \mathbf{F}_{LH} - \mathbf{F}_{L\alpha}, \tag{46}$$

$$M_H \ddot{\mathbf{r}}_H = -\mathbf{F}_{LH} - \mathbf{F}_{H\alpha}, \tag{47}$$

$$m_\alpha \ddot{\mathbf{r}}_\alpha = \mathbf{F}_{L\alpha} + \mathbf{F}_{H\alpha}. \tag{48}$$

Here we assumed that the two heavy fragments have the same multipolarity in deformations. Presently we consider only quadrupole deformations.

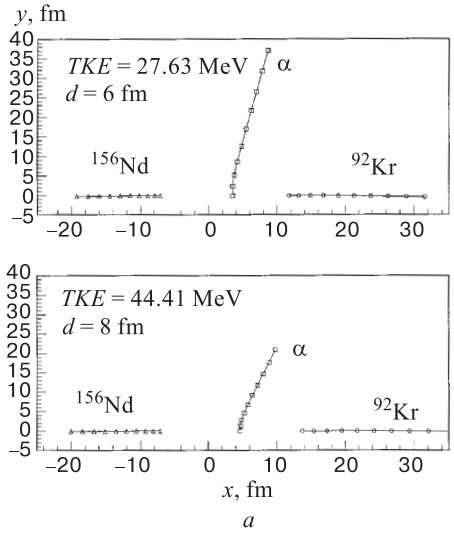

a

Fig. 23. The trajectory of the three fragments for the splitting a) ^{96}Kr + ^{152}Nd, b) ^{104}Mo + ^{144}Xe, and c) ^{116}Pd + ^{132}Sn

After solving numerically the above system of ordinary differential equations we are able to compute relevant quantities from the experimental point of view like the final angular distribution and final kinetic energies of the three fragments.

In Fig.23 we present the trajectories of the three fragments for the two extreme initial conditions (with high and with low kinetic energies of the heavier fragments) in a sequence of 10 time steps. The time scale is divided into increments of $\Delta t = 1.8\times 10^{-22}$. In Fig.23a we display the trajectories of one of the most asymmetric splittings, recorded in experiment, i.e., ^{156}Nd + ^{92}Kr. Since in this case the α feels a stronger repulsion from the heavy fragment, it will be deflected at a larger angle in the direction of the light fragment. In the case of the splitting ^{144}Xe + ^{104}Mo this deflection will be less pronounced (Fig.23b) and for the more equilibrated splitting, i.e., ^{132}Sn + ^{116}Pd, the α will be only slightly deflected (Fig.23c). We thus observe that in all the cases the α particle is deflected in the direction of the light fragment, but with a larger angle when the initial kinetic energy of the heavier fragments is higher. This fact should be attributed to the low energy of the α ($\leq$ 1MeV) which makes it to feel for a longer time the repulsion coming from the heavy fragment. In Ref.50 we computed the final kinetic energies E_α^f and the asymptotic angles θ_α^f for the three splittings mentioned above when we employ point-like and size dependent forces. In all cases we observe the decreasing of E_α^f with increasing tip distance d. Apparently, the phenomenon of α-particle energy *amplification* in the cold fission seems to

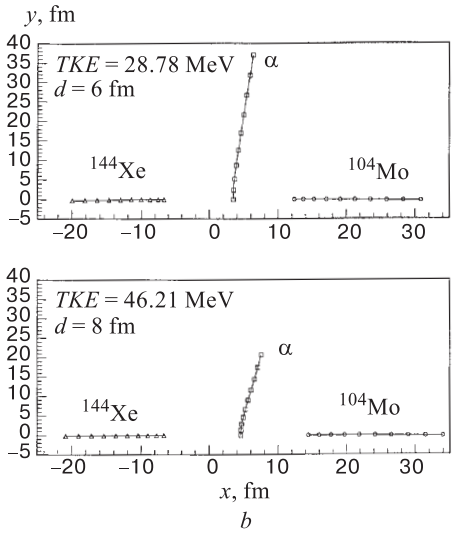

Fig. 23*b*

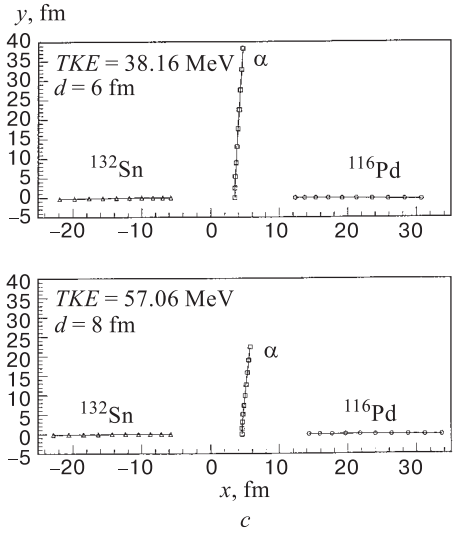

Fig. 23*c*

follow the same pattern like in normal fission. This effect should be attributed solely to the predominant effect of the *electric field lenses* and less to deformation or finite size effects. It should also be remarked the near constancy of the

final α kinetic energy for different mass splittings at the same tip distance, a fact already remarked long time ago in spontaneous fission [43]. In what concerns the angles at which α particles are emitted, their dependence on the mass splitting is obvious. Deviations from the axis perpendicular to the fission axis increase with the mass ratio. The difference observed between the two sets of data points to an important influence of the geometrical factors, which however does not alter the general trends of the process.

There are available experimental data on the α (and other particles) spectra, as a function of the total excitation energy, reaching TXE = 10 MeV within the experimental accuracy performed by the Darmstadt group with the DIOGENES set-up, and in a more recent work at the MPI Heidelberg [51]. These data do not contain special effects in the alpha spectra, when the cold fission regime is approached, except that the mean energy of the α increases nearly linearly with decreasing TXE. This would mean that if the linear dependence is extrapolated to TXE = 0 MeV, the average kinetic energy of the α will approach the value ($\approx$ 18.7 MeV) [52]. The fact that the experimental value is slightly higher than in hot fission (15.9 MeV) is a sign that the α is emitted earlier in cold fission, according to the uncertainty relation for energy $\Delta E \cdot \Delta t \approx \hbar$.

According to the calculations presented above, a range between 12 to 20 MeV should be expected for the final kinetic energy if we consider that the α particle occupies the lowest states in the pocket formed from the interaction with the two heavier fragments.

The experiment can be reconciled with our calculations if we suppose that the α is emitted before the pocket disappears, i.e., if the emission takes place between 6 and 7 fm tip distance.

As has been pointed by Halpern [43], there is no reason to believe that the third-particle ejection rates should be independent of the initial angular momentum. In our case, the spin of the parent nucleus (^{252}Cf) being zero, the angular momentum is imparted to the fragments and their relative angular momentum is mainly due to the creation of a molecular configuration at the scission point [53]. In the model presented above, we did not took into account the influence of collective molecular excitations, like bending or wriggling, nor the torques exerted between the fragments during quasi-classical motion [47].

5. DISCUSSION AND CONCLUSIONS

In the frame of a cluster model which includes quadrupole, octupole and hexadecupole deformations, we studied the spontaneous binary and ternary cold fission of the nucleus ^{252}Cf.

The calculations carried out for the binary cold fission confirmed the existence of two distinct regions where this process is enhanced. The results indicate two

different mechanisms. In the heavy-mass region situated between 138 and 156, the hexadecupole deformation gives rise to a large number of splittings. Here the shell closure in neutrons or protons seems to not be involved. Although the shell effects should play an important role in the odd-even differences by enhancing the odd-odd mass splits with respect to the even-even one, our results emphasize that the fragments are emitted with the deformations corresponding to those of the ground state. In the spherical region our results give only a hint of the importance of the magic nucleus ^{132}Sn which is susceptible to be produced in a heavy clusterization process, similar to that for light clusters. Here the decay mechanism should be similar to the light cluster radioactivity, the daughter nucleus ^{132}Sn being traded for ^{208}Pb and the heavy cluster ^{120}Cd for ^{14}C.

Based on a three-body cluster model, we studied the alpha ternary cold (neutronless) fragmentations of ^{252}Cf. Two regions of cold fission yields were obtained: one corresponding to large fragment deformations and another one to spherical fragments, like in the case of binary fragmentation. It is worthwhile to mention that based on the existing experimental data on cold alpha ternary yields [17] we expect that the first region contains the main cold fission yields and that the second region represents only few percents of the whole process. From the structure of the three body potential only few scenarios are possible all of them related to the initial position of the α particle in the equatorial plane. Only for the Lagrange scenario which corresponds to the alpha particle situated on the top of the alpha barrier, we found that the cold alpha ternary yields of ^{252}Cf are strongly correlated with the cold binary yields of the daughter nucleus ^{248}Cm. For all other considered scenarios, adiabatic and some excited states in the interfragment ridge well, the alpha ternary cold fission yields are existing mainly for the splittings with one spherical fragment. Due to the fact that there are experimental data for both regions, we conclude that only the Lagrange scenario can describe the cold alpha ternary process. We should mention also that the cold fission yields depend dramatically on some parameters like diffusivity a. If we choose larger a values for the deformed nuclei than for spherical ones, we can enhance drastically the corresponding yields. Also by choosing larger values for diffusivity for odd-even fragmentations than for even-even fragmentations, we obtain a larger odd-even effect. We expect the largest yield for odd-even and odd-odd fragmentations. Evidently, such effects must exist for excited states when the level density is important. Further experimental data are necessary in order to clarify such effects.

We computed the final kinetic energies of the fragments emitted in the α accompanied cold fission of ^{252}Cf taking into account the ground state quadrupole deformation and the finite-size effects of the fragments and integrating the equations of motion for a three-body system subjected only to Coulomb forces. The comparison with the available experimental data points to an earlier emission of the light particle in the cold fission.

A striking feature of the cold fission yields close to the highest TKE values permitted by the Q-values is the fact that many odd-odd splittings have values larger than the neighbouring even-even fragmentations. This feature of cold fragmentations suggests that either the cold fission yields are strongly influenced by the level density of the fragments or that the deformations of odd-dd fragments, possibly the triaxial ones, are larger than those corresponding to even-even ones.

The recent observation of ^{10}Be accompanying the ternary cold fission of ^{252}Cf opened the interest to search for possible molecular states in cold fragmentation processes. The possible occurence of such collective excitations is supported by the fact that cold fission is just a natural extension of cluster radioactivity to heavy nuclei.

REFERENCES

1. **Săndulescu A., Greiner W.** — Rep. Prog. Phys., 1992, v.55, p.1423.
2. **Price P.B.** — Nucl. Phys., 1989, v.A502, p.41c.
3. **Hambsch F.-J., Knitter H.-H., Budtz-Jorgensen C.** — Nucl. Phys., 1993, v.A554, p.209.
4. **Benoufella A. et al.** — Nucl. Phys., 1993, v.A565, p.563.
5. **Hamilton J.H. et al.** — J. of Phys. G: Nucl. Part. Phys., 1994, v.20, p.L85.
6. **Ter-Akopian G.M. et al.** — Phys. Rev. Lett., 1994, v.73, p.1477.
7. **Săndulescu A. et al.** — Phys. Rev., 1996, v.C 54, p.258.
8. **Săndulescu A. et al.** — Phys. Rev., 1998, v.C 57, p.2321.
9. **Schwab W. et al.** — Nucl. Phys., 1994, v.A577, p.674.
10. **Săndulescu A., Greiner W.** — J.of Phys. G : Nucl. Phys., 1977, v.3, p.L189.
11. **Milton J.C.D., Fraser J.S.** — Can. J. Phys., 1962, v.40, p.1626.
12. **Guet C. et al.** — Nucl. Instr. and Meth., 1978, v.150, p.189.
13. **Berger J.F., Girod M., Gogny D.** — Nucl. Phys., 1984, v.A 428, p.23c.
14. **Săndulescu A., Florescu A., Greiner W.** — J. of Phys. G: Nucl. Part. Phys., 1989, v.15, p.1815.
15. **Gönnenwein F., Börsig B.** — Nucl. Phys., 1991, v.A530, p.27.
16. **Florescu A. et al.** — J. of Phys. G:Nucl. Part. Phys., 1993, v.19, p.669.
17. **Ramayya A.V. et al.** — Phys. Rev., 1998, v.C 57, p.2370.
18. **Ter-Akopian G.M. et al.** — In: Fission and Properties of Neutron-Rich Nuclei, eds.J.H.Hamilton and A.V.Ramayya, World Scientific, Singapore, 1998, p.165.
19. **Satchler G.R., Love W.G.** — Phys. Rep., 1979, v.55, p.183.
20. **Möller P. et al.** — At. Data and Nucl. Data Tables, 1995, v.59, p.185.
21. **Săndulescu A. et al.** — Int. J. of Mod. Phys., 1992, v.E 1, p.379.
22. **Carstoiu F., Lombard R.J.** — Ann. of Phys. (N. Y.), 1992, v.217, p.279.
23. **Bertsch G. et al.** — Nucl. Phys., 1977, v.A284, p.399.
24. **Brandan M.E., Satchler G.R.** — Phys. Rep., 1997, v.285, p.143.

25. **Adamian G.G. et al.** — Int.J.of Mod.Phys., 1996, v.E 5, p.191.
26. **Mişicu Ş., Protopopescu D.** — JINR preprint E4-98-179, Dubna, 1998.
27. **Hirschfelder J.O., Curtiss C.F., Bird R.B.** — Molecular Theory of Gases and Liquids,, John Willey & Sons, 1954.
28. **Wapstra A.H., Audi G., Hoeckstra R.** — At. Data and Nucl. Data Tables, 1988, v.39, p.281.
29. **Möller A. et al.** — In: Int.Conference on Large Scale Collective Motion of Atomic Nuclei, Brolo, 1996.
30. **Gönnenwein F. et al.** — Il Nuovo Cimento, 1997, v.110 A, p.1089.
31. **Crönni M. et al.** — In: Fission and Properties of Neutron-Rich Nuclei, Eds.Hamilton J.H. and Ramayya A.V., World Scientific, Singapore, 1998, p.109.
32. **Avrigeanu V. et al.** — Phys. Rev., 1995, v.C 52, p.R1755.
33. **Dilg W. et al.** — Nucl.Phys., 1973, v.A217, p.269.
34. **Săndulescu A. et al.** — J.Phys.G: Nucl.Part.Phys., 1998, v.24, p.181.
35. **Razavy M., Pimpale A.** — Phys. Rep., 1988, v.168, p.305.
36. **Radi H.M.A. et al.** — Phys.Rev., 1982, v.C 26, p.2049.
37. **Ramayya A.V. et al.** — In: Dynamical Aspects of Nuclear Fission, Proceedings of 3rd Int. Conf., Casta-Papiernicka, Slovak Republic, August 30 — September 4, 1996, Eds. Kliman J. and Pustylnik B., Dubna, 1996, pp.307.
38. **Hamilton J.H. et al.** — Prog. Part. Nucl. Phys., 1997, v.38, p.273.
39. **Ramayya A.V. et al.** — Phys.Rev.Lett., 1998, v.81, p.947.
40. **Singer P. et al.** — In: Dynamical Aspects of Nuclear Fission, Proceedings of 3rd Int. Conf., Casta-Papiernicka, Slovak Republic, August 30 — September 4, 1996, Eds. Kliman J. and Pustylnik B., Dubna, 1996, pp.262.
41. **Geilikman B.T., Hlebnikov G.I.** — At.Energiya, 1965, v.18, p.218.
42. **Boneh Y., Fraenkel Z., I. Nebenzahl I.** — Phys.Rev., 1967, v.156, p.1305.
43. **Halpern I.** — Ann.Rev.Nucl.Sci., 1971, v.21, p.245.
44. **Ertel P.** — In: Statistical Theory of Nuclear Fission, ed.Fong P., Gordon and Breach, Science Publishers, Inc., New York, 1969, pp. 191-126.
45. **Fong P.** — Phys.Rev., 1970, v.C 2, p.735.
46. **Choudhury R.K., Ramamurthy V.S.** — Phys.Rev., 1978, v.C 18, p.2213.
47. **Cârjan N., Leroux B.** — Phys.Rev., 1980, v.C 22, p.2008.
48. **Pik-Pichak G.A.** — Sov.J.Nucl.Phys., 1984, v.40, p.215.
49. **Davies K.T.R., Sierk A.J., Nix J.R.** — Phys.Rev., 1976, v.C 13, p.2385.
50. **Mişicu Ş.** — JINR preprint E4-98-121 Dubna, 1998.
51. **Mutterer M. et al.** — In: Dynamical Aspects of Nuclear Fission, Proceedings of 3rd Int. Conf., Casta-Papiernicka, Slovak Republic, August 30 — September 4, 1996, Ed. by.Kliman J. and Pustylnik B., Dubna, 1996, p.250.
52. **Mutterer M., Kopach Y.** — Private communication (1998).
53. **Mişicu Ş., Săndulescu A., Greiner W.** — Mod.Phys.Lett., 1997, v.A 12, p.1343.